Chapter 2

The Role of Extended Defects During Semiconductor Processing

2.1 Introduction

Ion implantation, by its very nature, introduces crystal damage to the target material. This damage is predominantly in the form of point defects, interstitials and vacancies. We now know that the behavior of these point defects during subsequent annealing strongly influences dopant diffusion until the defect concentrations return to their equilibrium values. For implant doses above the amorphization threshold, category II damage, also called end-of-range damage, is created during subsequent annealing [8]. Kim *et al.* [9] and Fair [10] have reported reduced oxidation-enhanced diffusion (OED) of phosphorus after an amorphizing implant. They postulated that the end-of-range damage created by the amorphizing implant absorbs some of the excess interstitials injected by oxidation, resulting in less OED of the phosphorus. This chapter focuses on the effect of these extended defects during subsequent processing, specifically during thermal oxidation and additional implant-damage enhanced diffusion (IED). By monitoring the diffusion of a boron marker layer using secondary ion mass spectrometry (SIMS) and by monitoring the evolution of the extended defects via transmission electron microscopy (TEM), we have shown that these extended defects absorb excess interstitials reducing OED and IED.

Using the data for reduced OED at 900ßC, we calculate bounds on the $D_I C_I^*$ product and θ_{net} where D_I is the interstitial diffusivity, C_I^* is the equilibrium interstitial concentration and θ_{net} is the net number of interstitials injected during the oxidation. We then describe a one-dimensional model for dislocation loop growth which we have implemented into SUPREM-IV. Simulations using the new model are compared to experimental data.

2.2 Effects of Extended Defects During Thermal Oxidation

2.2.1 Experimental Procedure

The starting material was either 4-inch, <100>, phosphorus doped, float-zone (FZ) silicon with a resistivity of 5.3-6.1 Ω-cm or 4-inch, <100>, phosphorus doped, Czochralski (CZ) silicon with a resistivity of 5-10 Ω-cm. Epitaxial silicon was used to grow boron marker layers between 0.25-0.4 μm thick with a peak concentration of $2x10^{18}$ cm^{-3}. Epitaxial growth was continued for another 0.8-1.3 μm to grow a lightly-doped arsenic buffer layer on top of the boron marker layer. A thick, low temperature oxide was then deposited. Lithography and wet etching were used to define exposed and masked regions. The wafers were implanted with Si^{28} at an energy of 100 keV and a dose of $1x10^{15}$ cm^{-2}. The CZ wafers received an additional Si^{28} implant at an energy of 50 keV and a dose of $1x10^{15}$ cm^{-2}. Samples were rapid thermal annealed for 1 minute at 1050ßC, and then the masking oxide was stripped using buffered hydrofluoric (HF) acid. The enhanced diffusion due to the implant damage should be over after this high temperature anneal. At this point, the wafers were cleaved into halves, half of each wafer was set aside for initial profile measurements, and the other half was oxidized at 850ßC, 900ßC, 950ßC, or 1000ßC in pyrogenic steam for various times. The thicknesses of the oxides grown were measured using an interferometer. The oxides were etched off, and the initial and final boron profiles were measured with SIMS using an oxygen primary ion beam in a Cameca IMS-3f or 4f system. A summary of the process flow is given in Figure 2.1.

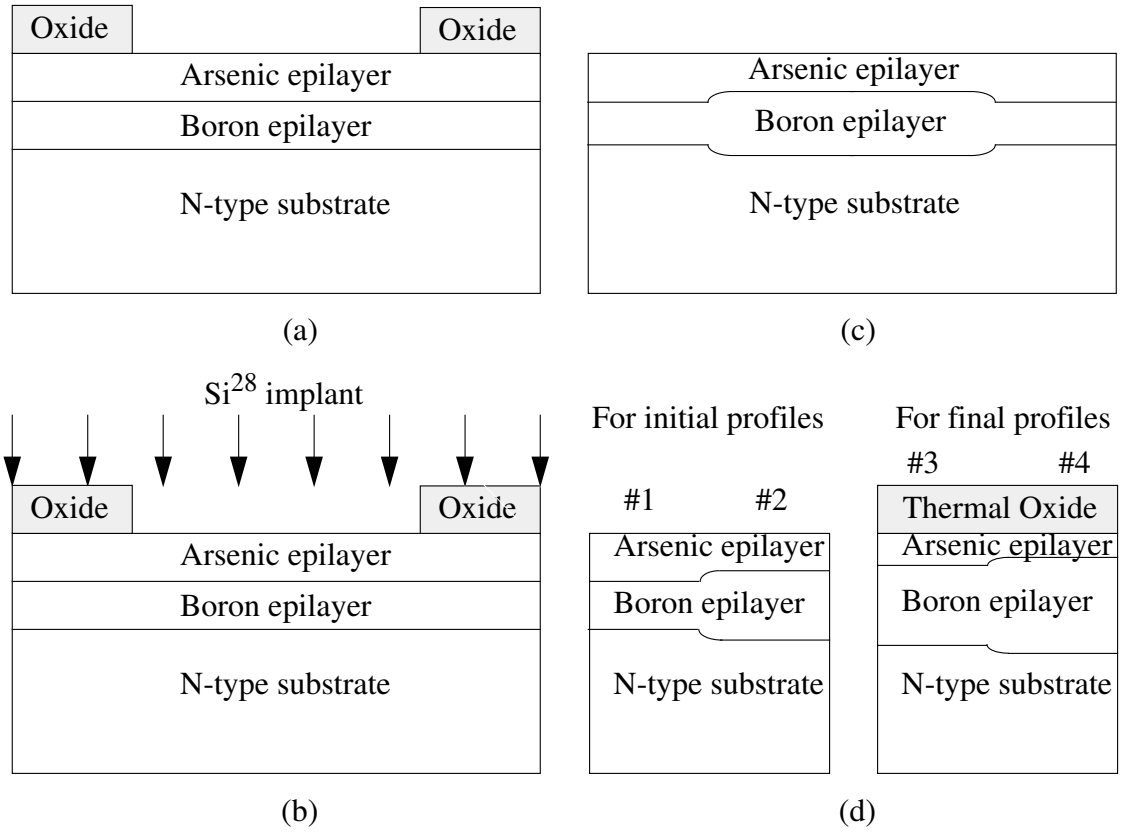

Figure 2.1 Process flow for reduced OED study. (a) n-type starting material, boron/ arsenic epi growth, oxide deposition, and lithography. (b) High-dose Si^{28} implant. (c) Oxide etch, 1050ßC, 1 minute RTA. (d) Wafers cleaved in halves. Half saved for initial profile (left side) and half oxidized in pyrogenic steam (right).

2.2.2 Experimental Results

Figure 2.2 shows the boron profiles before and after a 2 hour wet oxidation at 900ßC. Due to IED, the starting profile underneath the region implanted with silicon is broader than the profile underneath the masked region. However, after oxidation, the boron profile is now narrower in the region implanted with silicon as compared to the masked region. SUPREM-IV was used to determine the amount of enhanced boron diffusion that occurred during the oxidation by diffusing the initial SIMS profile into the final SIMS profile for each oxidation condition and for both implanted and masked regions. The default boron diffusivity in SUPREM-IV [7] was increased by constant multiplicative factors until the

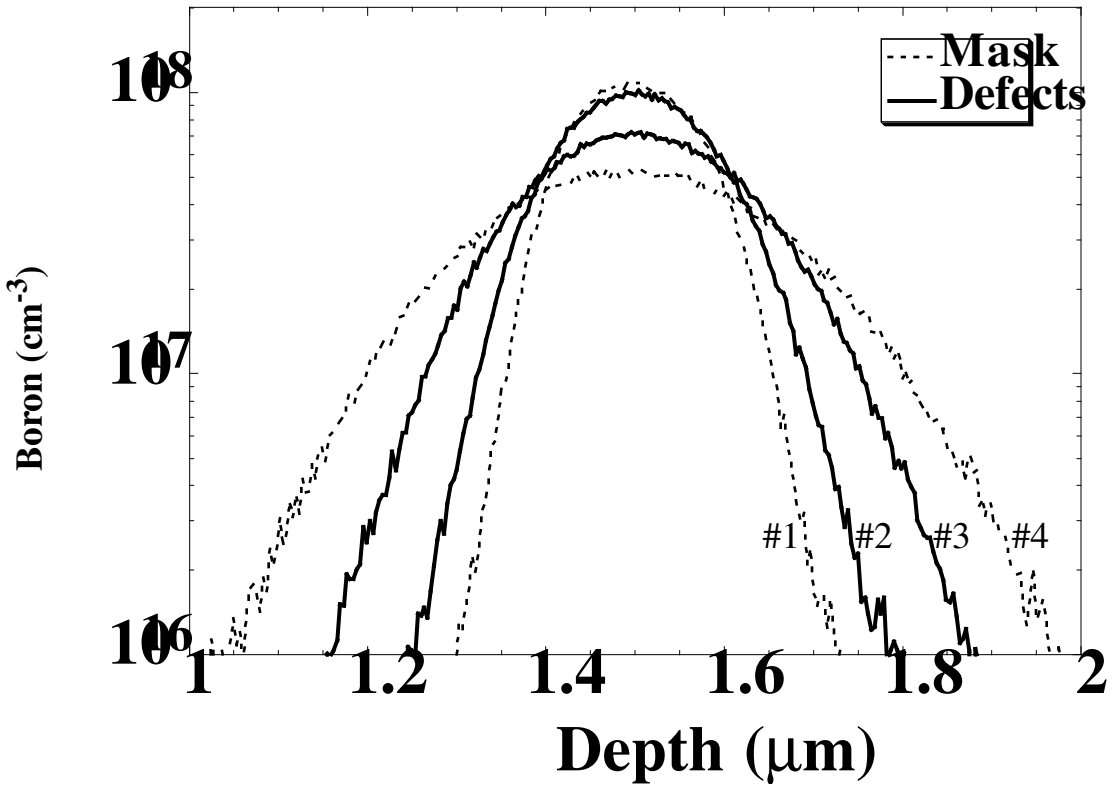

Figure 2.2 SIMS data before (Curves #1 and #2) and after (Curves #3 and #4) oxidation for the 900ßC, 2 hour oxidized sample. The solid lines are the profiles underneath a region with defects, and the dotted lines are the profiles underneath a region without defects. The curves are numbered following the convention in Figure 2.1(d).

final simulated profile matched the experimental data. The extracted enhancements are given in Table 2.1 and show that high-dose implants are effective at reducing OED with larger reductions at lower temperatures. Also shown in Table 2.1 are the measured oxide thicknesses for the different samples. The measured oxide thicknesses agree quite well in both implanted and masked regions indicating that the oxidation kinetics were identical. The amount of normal OED measured at 900ßC in this experiment agrees very well with Packan s OED data [11] while the value measured at 1000ßC is approximately 50% higher.

The reduction in OED is due to the absorption of some injected interstitials by extended defects generated by the high-dose silicon implant. These extended defects are

usually centered at the original amorphous silicon/crystalline silicon interface. Channeling Rutherford Backscattering analyses on as-implanted samples showed that these silicon implant conditions generated amorphous layers 0.175 μm thick. In order to verify that these defects caused the reduced OED, TEM analysis was done on the 900ßC, 2 hour oxidized sample before and after oxidation. The plan-view TEMs shown in Figure 2.3 verify the existence of extended defects. The presence of interference fringes and the aspect ratio of the defects are consistent with extrinsic dislocation loops, extra planes of silicon atoms lying on {111} planes [8]. Although the density of dislocations decreases slightly during oxidation, the increase in average loop size results in a net increase in the number of interstitials bound by the dislocation loops.

Temp (ßC)	time (min.)	Extended Defects?	Oxide Thickness ( )	<D>/D*
850	120	No Defects	1361	24.4
850	120	Defects	1384	4.9
850	180	No Defects	1907	24.0
850	180	Defects	1904	5.1
900	120	No Defects	2399	14.8
900	120	Defects	2423	4.7
950	45	No Defects	1899	11.4
950	45	Defects	1884	6.5
1000	30	No Defects	2128	11.9
1000	30	Defects	2117	7.1

Table 2.1 Final oxide thicknesses and extracted enhancements for boron diffusivity during wet oxidation at various temperatures, with and without extended defects. D* is the default value for inert boron diffusivity in SUPREM-IV [7].

2.2.3 Calculation of $D_I C_I^*$ at 900ßC

Figure 2.4 (a) is a diagram of the interstitial fluxes present during the oxidation with extended defects. J_{total} represents the flux of interstitials into the silicon substrate due to the oxidation, J_{loops} represents the flux of interstitials into the extended defects, and J_{bulk}

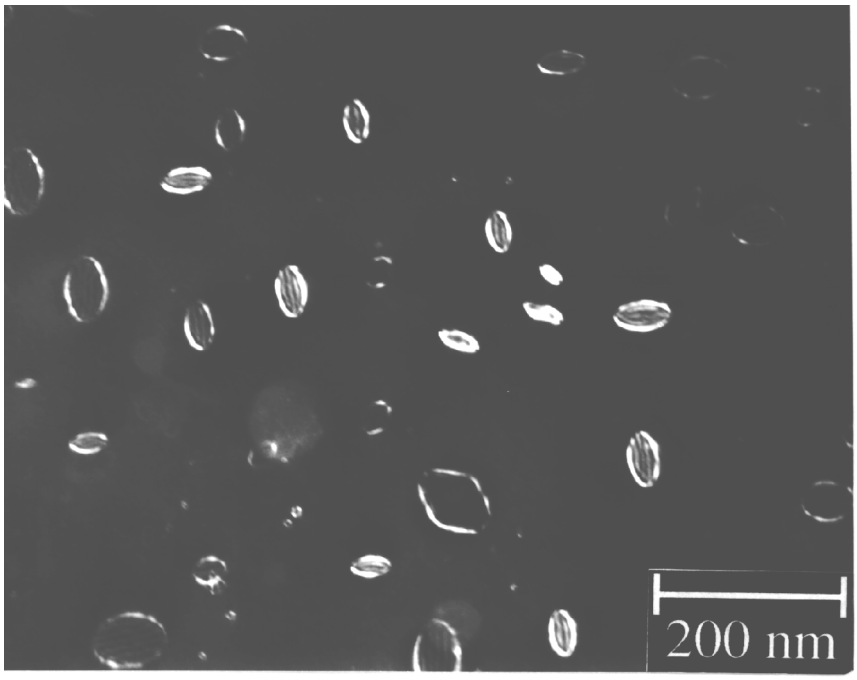

(a)

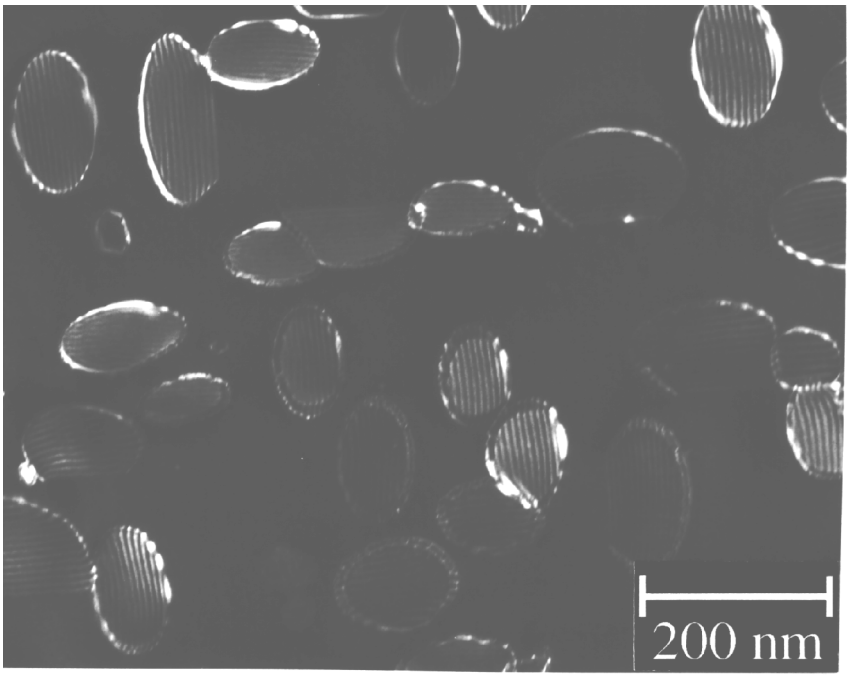

(b)

Figure 2.3 Plan-view TEM analysis samples (a) before and (b) after the 900ßC, 2 hour wet oxidation.

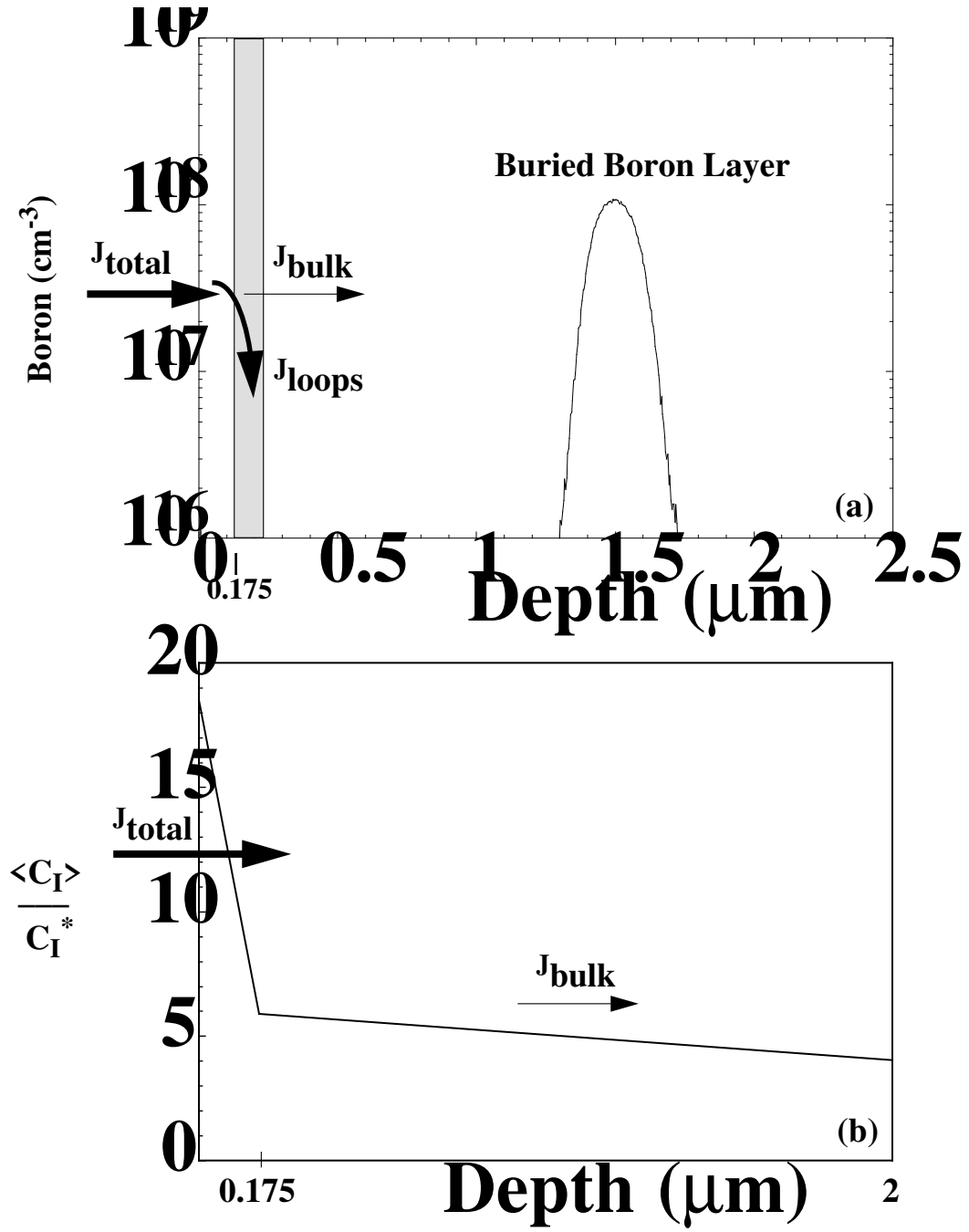

Figure 2.4 (a) Interstitial flux diagram during the wet oxidation. J_{total} is the flux due to the oxidation, J_{loops} is the flux into the extended defects, and J_{bulk} is the flux into the bulk of the substrate that enhances the diffusion of the boron buried layer. (b) Time-averaged interstitial supersaturations at various depths which are used to calculate J_{total} and J_{bulk}.

represents the flux of interstitials that penetrate into the remainder of the substrate. Only J_{bulk} affects the diffusion of the boron buried layer between 1 and 2 μm. An important note is that any interstitial flux due to recombination with vacancies is not accounted for in Figure 2.4 (a). Thus the $D_I C_I^*$ product which we calculate in this section will be an effective value. The total number of interstitials injected during the oxidation must be equal to the number of interstitials absorbed by the loops plus the number of interstitials that enhance the diffusion of the boron layer. If we use a quasi-steady state approximation (i.e. C_I within the layer of dislocation loops does not change with time), we can write:

$$J_{total} = J_{loops} + J_{bulk} \tag{2.1}$$

Figure 2.4 (b) shows the interstitial supersaturation for the case in which the defects are present. J_{total} and J_{bulk} can be calculated from the enhancements in boron diffusivity given in Table 2.1 by simply evaluating the diffusion flux in one-dimension using:

$$J = -(D_I C_I^*) \frac{ds_I}{dx} \tag{2.2}$$

s_I is the interstitial supersaturation ratio given by C_I/C_I^*. As shown in Section 1.3, in a dual point defect diffusion mechanism, the enhancement in boron diffusivity can be written as a function of the interstitial and vacancy supersaturation ratios:

$$\frac{\langle D_B \rangle}{D_B^*} = f_{BI} \times \frac{\langle C_I \rangle}{C_I^*} + (1 - f_{BI}) \times \frac{\langle C_V \rangle}{C_V^*} \tag{2.3}$$

where $\langle D_B \rangle$ is the time-averaged boron diffusivity, D_B^* is the inert boron diffusivity, f_{BI} is the fractional interstitial component of boron diffusion (approximately 0.8 [12]), $\langle C_I \rangle$ and $\langle C_V \rangle$ are the time-averaged interstitial and vacancy concentrations respectively, and C_I^* and C_v^* are the equilibrium interstitial and vacancy concentrations respectively. Ignoring any contribution to the enhanced diffusion due to vacancies ($\langle C_V \rangle / C_V^* = 1$) and solving for $\langle C_I \rangle / C_I^*$ gives:

$$\frac{<C_I>}{C_I^*} = \frac{1}{f_{BI}} \times \left(\frac{<D_B>}{D_B^*} - 1 \right) + 1 \tag{2.4}$$

Since the diffusion of the boron layer was found to be symmetric for all cases, we can assume that from the layer of dislocation loops down to 2 μm, the interstitial supersaturation is relatively flat. In Figure 2.4 (b), we also assume that regardless of whether the loops are present or not, the interstitial supersaturation at the silicon/oxide interface is identical in both cases. The value of the diffusivity enhancement without the defects from Table 2.1 (14.8X) along with Eq. 2.4 gives the first boundary condition, $s_I^{surface}$=18.25 where $s_I^{surface}$ represents the interstitial supersaturation at the growing interface. When the loops are present, the enhancement in boron diffusivity is only 4.7. This gives the second boundary condition, s_I^{loops}=5.625 where s_I^{loops} represents the interstitial supersaturation at the center of the layer of dislocation loops. Finally, we assume s_I will be unity at some depth, b, which is greater than 2 μm but less than 750 μm (the total thickness of the wafer).

Accounting for the change in loop density and average loop size from Figure 2.3 (a) to (b), and using the {111} planar density (1.57×10^{15} cm^{-3}), the number of silicon atoms absorbed by the dislocation loops was calculated. J_{loops} is then simply this number divided by the total time of the oxidation which was 2 hours.

We can calculate the $D_I C_I^*$ product by substituting Eq. 2.2 into Eq. 2.1 with the appropriate boundary conditions and assuming the interstitial supersaturation varies linearly with depth (see Figure 2.4(b)):

$$-D_I C_I^* \left(\frac{s_I^{loops} - s_I^{surface}}{a} \right) = J_{loops} - D_I C_I^* \left(\frac{1 - s_I^{loops}}{b} \right) \tag{2.5}$$

where a is the average distance from the surface to the center location of the loops (0.175 μm) since the silicon/oxide interface is constantly moving with time. Solving for $D_I C_I^*$ yields:

$$D_I C_I^* = \frac{J_{loops}}{\left(\frac{s_I^{surface} - s_I^{loops}}{a} - \frac{s_I^{loops} - 1}{b} \right)} \tag{2.6}$$

From the TEMs, $J_{loops} = 8.86 \times 10^{10}$ $cm^{-2}s^{-1}$. Approximately 1070 of silicon was consumed during the oxidation, so a = (1750 + 680)/2 = 1215 . Since 2 μm ≤ b ≤ 750 μm, we have a bound on $D_I C_I^*$ at 900ßC:

$$8.5x10^4 \le D_I C_I^* \ (cm^{-1}s^{-1}) \le 8.7x10^4 \tag{2.7}$$

This result is in very good agreement with Stolwijk s value [13] extracted from gold diffusion experiments:

$$D_I C_I^* = 3.2 \times 10^{25} exp\left(-\frac{4.8}{kT}\right) \tag{2.8}$$

which at 900ßC is 7.7×10^4 $cm^{-1}s^{-1}$. Another important point is that the flux into the bulk contributes very little to the total flux. Most of the interstitial flux due to the oxidation is accounted for by the flux into the dislocation loops. This is why the $D_I C_I^*$ product is virtually independent of b.

2.2.4 Calculation of θ_{net} at 900ßC

From the data in Figure 2.2, Figure 2.3, and Table 2.1, we can also calculate a minimum value for θ_{net}, the fraction of interstitials consumed during the oxidation which diffuse into the substrate. From the plan-view TEMs, we already know the number of interstitials absorbed by the loops. Integrating over time, we can calculate the number of interstitial atoms that enhance the diffusion of the boron buried layer. The total number of interstitials injected into the bulk is:

$$N_{inj} \ge N_{loops} + \int J_{bulk} dt \tag{2.9}$$

This equation does not account for any interstitials which recombine with vacancies. Thus we can only calculate a lower bound on θ_{net}. We showed in the last section that $J_{loops} >> J_{bulk}$, so we can ignore the second term on the right-hand side of Eq. 2.9. The total number of silicon atoms consumed is calculated from the measured oxide thicknesses in Table 2.1, the volume difference between oxide and silicon and the volume density of silicon, and is found to be approximately $5.3x10^{17}$ cm^{-2}. Thus,

$$\theta_{net} \geq \frac{N_{loops}}{N_{consumed}} = \frac{6.4x10^{14}}{5.3x10^{17}} = 0.0012 \qquad (2.10)$$

θ_{net} is found to be much less than one, which is physically correct. Only a very small fraction of the silicon atoms consumed are injected into the bulk as interstitials.

2.2.5 Model for dislocation loop growth

In our previous work [14], we effectively modeled the absorption of interstitials by the dislocation loops by adding the localized term $K_{int}(C_I-C_I^*)$ to the interstitial continuity equation. The sink was active only for $C_I > C_I^*$ and only within a constant, predetermined region. In this section, we describe a more physical one-dimensional model for the growth of dislocation loops which we implemented into SUPREM-IV. The interstitial continuity equation is modified accordingly to account for interstitials which are lost to the dislocation loops. The dissolution of loops and concurrent supersaturation of interstitials can also be described by this model. Simulation results using the new model are compared to the current data set.

Modeling the growth of oxidation-induced stacking faults (OSFs) has been an active area of research over the last two decades [15]-[17]. The fact that OED has been observed in conjunction with the growth of OSFs has led to the generally accepted theory that OSFs grow by absorbing interstitials. Experimentally, stacking fault growth is independent of the spacing between the faults, i.e. their density, indicating that stacking fault growth does not reduce interstitial supersaturation and so is predominantly a reaction-controlled process [16],[18].

The dislocation loops generated by ion implantation damage also bound stacking faults, the difference being the implant-induced stacking faults (ISFs) are much smaller than OSFs. Although, it is not known a priori whether or not ISF growth is diffusion-controlled, reaction-controlled, or a combination of both, we will first implement a model for ISF growth assuming the process is reaction-limited, match our experimental results with the model, and then go back to assess the validity of our assumption.

The volume surrounding a dislocation line bounding a stacking fault can be approximated by a torus. Hu [16] accounts for the reaction energy barrier to stacking fault growth in the following equation:

$$\frac{dr}{dt} = \left(\frac{\pi}{N_o}\right)\left(\frac{r_t}{r_a}\right)^2 D_I exp\left(\frac{-\Delta H}{kT}\right)\left(C_C - C^*_{I,\,loop}\right) \tag{2.11}$$

where the parameters are defined as follows:

r: stacking fault radius
N_o: {111} planar density
r_t: radius of torus surrounding outer edge of the stacking fault
r_a: interatomic spacing of the silicon lattice
C_C: interstitial concentration at the surface of the torus
$C^*_{I,loop}$: equilibrium interstitial concentration within the torus
D_I: interstitial diffusivity
ΔH: reaction energy barrier for loop growth
k: Boltzmann s constant
T: temperature in degrees Kelvin

Figure 2.5 illustrates the dislocation loop geometry as well as the interstitial concentrations of interest.

Equation 2.11 was implemented into SUPREM-IV to solve for the average dislocation loop radius as a function of time. SUPREM-IV solves the continuity equation for interstitials (Eq. 2.13) and generates the interstitial concentration as a function of both time and space. The value calculated at the layer of dislocation loops is used for C_C in Eq. 2.11. $C^*_{I,loop}$ will be greater than the usual interstitial equilibrium concentration because

Figure 2.5 Schematic representation of the torus surrounding the stacking fault along with the interstitial concentrations of interest. r is the radius of the stacking fault, and r_t is the radius of the torus surrounding the stacking fault. C_C is the interstitial concentration on the surface of the torus, C_I^{∞} is the interstitial concentration far away from the dislocation loop, C_I^* is the bulk equilibrium interstitial concentration, and $C^*_{I,loop}$ is the equilibrium interstitial concentration within the torus surrounding the stacking fault.

of the extra energy associated with a dislocation loop (both strain and internal). An expression for $C^*_{I,loop}$ can be derived based on the energy associated with the dislocation loop. Kroupa [19] has derived an expression for the total energy of a circular, edge dislocation loop as a function of loop radius. Following Hu [16], but including the strain energy of the dislocation, $C^*_{I,loop}$ can be shown to be

$$C^*_{I,\,loop} = C^*_I \exp\left[\frac{\gamma\Omega}{bkT}\right]\exp\left[\frac{\mu b\Omega}{4\pi rkT(1-\nu)}\ln\left(\frac{8r}{b}\right)\right] \qquad (2.12)$$

where the parameters are defined as follows:

- γ: internal energy of the stacking fault (approximately 70 mJ/m^2 for silicon [20])
- Ω: volume per silicon atom
- b: magnitude of the Burger s vector for the dislocation loop (3.14 in this case)

μ: shear modulus

r: dislocation loop radius

ν: Poisson s ratio

$C^*_{I,loop}$ versus loop radius at 900ßC is plotted in Figure 2.6. Note that $C^*_{I,loop}$ is a strong

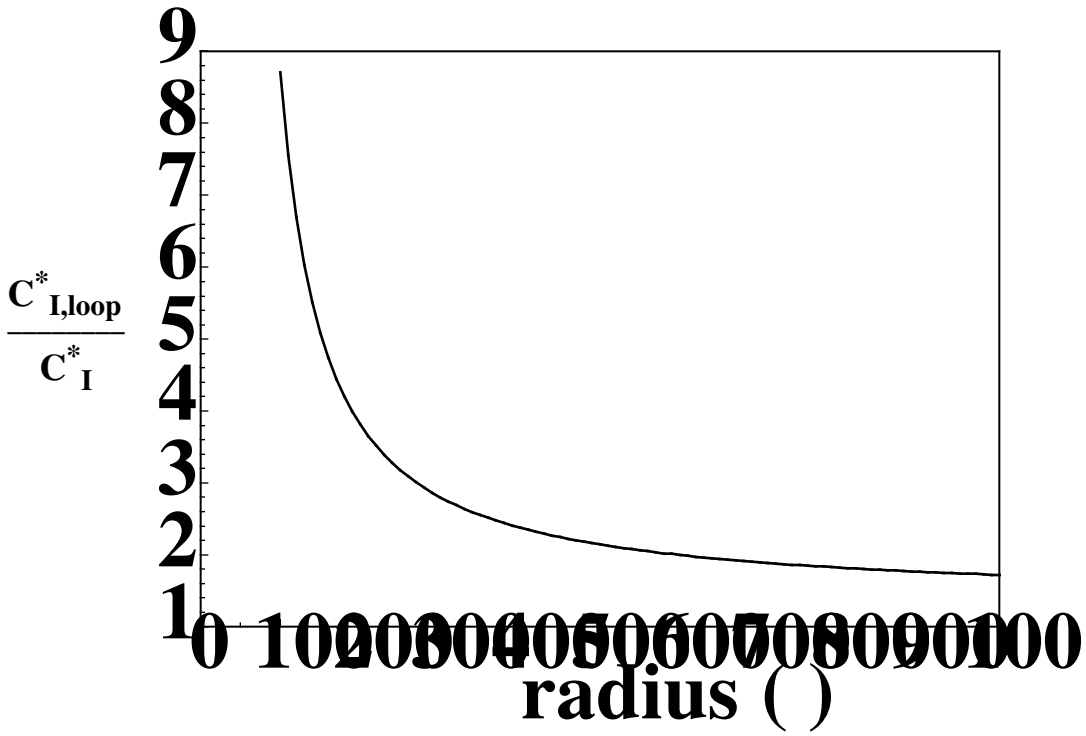

Figure 2.6 Equilibrium interstitial concentration surrounding a dislocation loop as a function of loop radius at 900ßC.

function of r at small radii, but is relatively constant for radii greater than 400 . This expression for $C^*_{I,loop}$ is the crucial factor in determination of whether or not the dislocation loop growth is a reaction or diffusion-limited process. If the growth is diffusion-limited, then C_I will be approximately $C^*_{I,loop}$ (in fact slightly higher to sustain loop growth). However, if the growth is reaction-limited, then C_I can be significantly larger than $C^*_{I,loop}$ as the reaction rate will not be able to keep up with the diffusion of interstitials to the loops.

The interstitial continuity equation was modified in a consistent manner with Eq. 2.11 to account for the interstitials absorbed by the dislocation loops. Each dislocation loop of

radius r increases in area by $2\pi r(dr/dt)$. The rate of interstitial absorption for one loop is then $N_o x 2\pi r(dr/dt)$. Multiplying by the areal density of the dislocation loops, ρ, gives the total number of interstitials absorbed per unit area as $\rho N_o x 2\pi r(dr/dt)$. Finally, dividing by the total thickness of the layer of dislocation loops (since the dislocations lie on {111} planes, this thickness is not 2r, but $2r/\sqrt{3/2}$) yields the number of interstitials absorbed per unit volume per unit time. Thus, in one-dimension, assuming D_I is constant, the interstitial continuity equation is:

$$\frac{\partial C_I}{\partial t} = D_I \frac{\partial^2 C_I}{\partial x^2} - R_{Bulk} - \sqrt{\frac{3}{2}}\pi^2 K_{loop} D_I \rho \, (C_I - C_{I,\,loop}^{*}) \tag{2.13}$$

where $(r_t/r_a)^2 \exp(-\Delta H/kT)$ has been grouped into the constant, K_{loop}. On the right hand side of Eq. 2.13, the first term is the diffusive flux, the second term accounts for bulk recombination, and the third term accounts for interstitial absorption by the dislocation loops. The center axes of all the loops are assumed to lie on the same plane at 0.175 μm from the original silicon surface, the original location of the amorphous silicon/crystalline silicon interface as measured using channeling RBS analysis. Type II dislocation loops are known to form at this location [8]. To first order, ρ can be assumed constant. In Figure 2.3, the loop density is 5.2×10^9 cm^{-2} before oxidation and 3.8×10^9 cm^{-2} after oxidation. Others have also found that loop density changes very little during both inert and oxidizing conditions [21],[22].

SUPREM-IV was used to solve Eq. 2.13 and an analogous equation for vacancies. The equation for vacancies only considers the diffusive flux and bulk recombination. The interstitials must satisfy the following boundary condition:

$$J_I \bullet \boldsymbol{n} + K_{ox}(C_I - C_I^{*}) = G = \frac{\theta v_i}{\Omega} \tag{2.14}$$

where J_I is the interstitial diffusion flux, G is the generation of interstitials at the growing interface, and v_i is the interface velocity. K_{ox} is the surface recombination velocity at the oxidizing interface and is modeled by:

$$K_{ox} = K_S^I \left[K_{rat} \left(\frac{v_i}{B/A} \right)^{0.5} + 1 \right] \quad (2.15)$$

where K_S^I is the recombination velocity at an inert oxide interface, K_{rat} reflects the increase in interstitial recombination velocity at an oxidizing interface, and B/A is the Deal-Grove linear rate oxide growth coefficient. The vacancies must satisfy an analogous boundary condition except that at the oxidizing interface, the generation of vacancies is assumed to be zero. After solving the coupled continuity equations for interstitials and vacancies, SUPREM-IV then solves the continuity equation for the dopant which for the case of boron is:

$$\frac{\partial C_B}{\partial t} = \nabla \left[D_{BV} C_B \frac{C_V}{C_V^*} \nabla ln \left(C_B \frac{C_V}{C_V^*} \frac{p}{n_i} \right) + D_{BI} C_B \frac{C_I}{C_I^*} \nabla ln \left(C_B \frac{C_I}{C_I^*} \frac{p}{n_i} \right) \right] \quad (2.16)$$

where $D_{BV}=(1-f_{BI})(D_B^0+D_B^+p/n_i)$ and $D_{BI}=f_{BI}(D_B^0+D_B^+p/n_i)$. D_B^0 is the contribution of boron diffusivity due to neutral defects, D_B^+ is the contribution of boron diffusivity due to singly, positively charged defects, C_B is the boron concentration, p is the hole concentration, and n_i is the intrinsic carrier concentration. The default values for D_B^0 and D_B^+ in SUPREM-IV [7] were used for all simulations.

2.2.6 Comparison of simulation results to experimental data at 900ßC

Having implemented the model for dislocation loop growth into SUPREM-IV, the following methodology was used to determine the optimal value for K_{loop} at 900ßC which would fit not only the reduced OED data, but also the TEM data. Extension of the model to the other temperatures will be discussed later. First of all, the amount of normal OED of the boron layer without extended defects is identical to the value obtained by Packan [11]. Griffin *et al.* [23] have recently been able to model both Packan s dry OED data and implant damage enhanced diffusion data with a single set of simulation parameters. This set of parameters was also used here, with the exception that the equilibrium interstitial concentration was increased such that the $D_I C_I^*$ product used in the simulations would be

equal to 8.6×10^4 $cm^{-1}sec^{-1}$ (which is the value calculated in Section 2.2.3 from the experimental data). Since the data in Table 2.1 is for a wet oxidation, the parameter θ is expected to be different from that given by Griffin *et al.* for dry oxidation. θ was varied to obtain a best-fit to the normal OED data. Next this same set of parameters and optimized θ was used to simulate the case where extended defects are present. K_{loop} was varied to obtain a best-fit to the reduced OED data.

Figure 2.7 shows the good match between experimental data and simulated result for

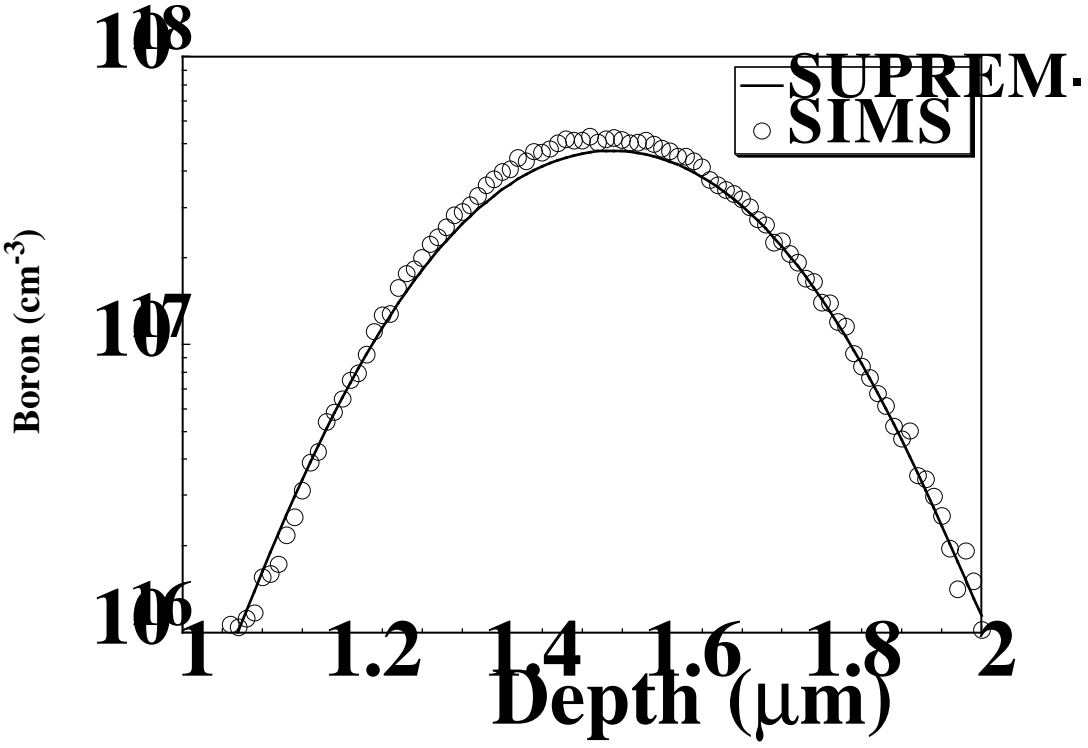

Figure 2.7 Comparison of the optimized, simulated boron profile versus SIMS data for the case of normal OED without extended defects.

the optimization of θ at 900ßC, and Table 2.2 lists the simulation parameters used. θ_{opt} was found to be 0.016 which is greater than the minimum value calculated for θ_{net} from Section 2.2.4. An average initial loop radius of 235 and an average dislocation loop density of 4.5×10^9 cm^{-2} was input to SUPREM-IV for the simulation with extended defects during the 900ßC wet oxidation. Figure 2.8 shows a good match between the experimental data and the optimized simulation result for K_{loop}. The optimal value for

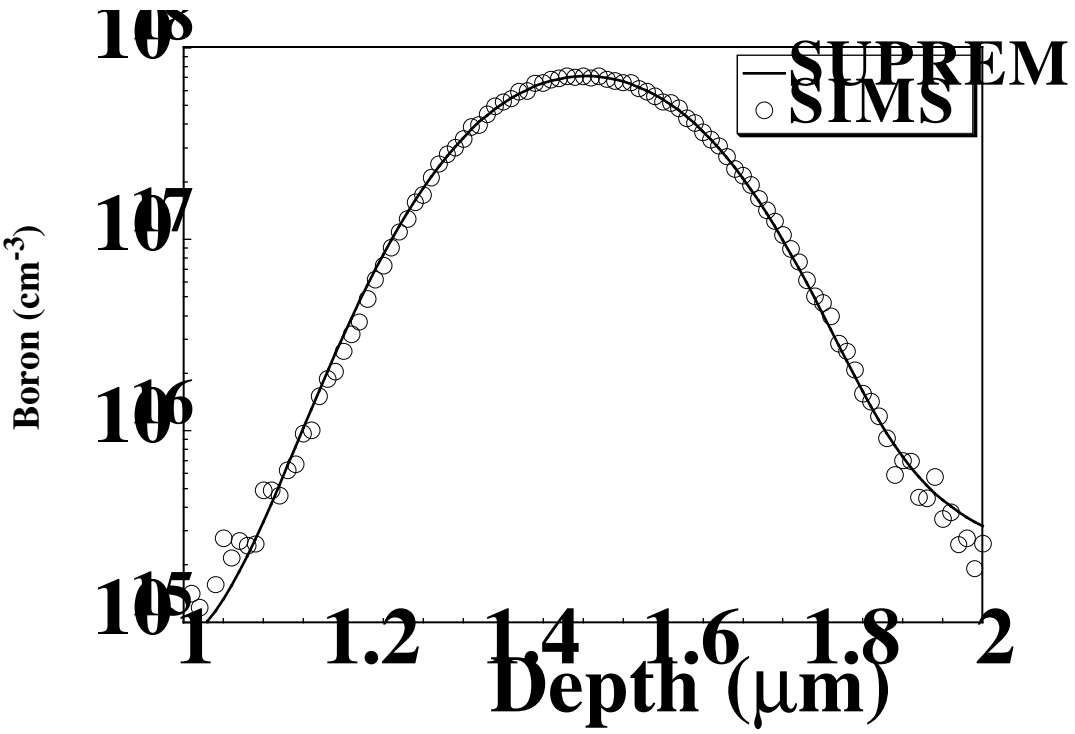

Figure 2.8 Comparison of the optimized, simulated boron profile (using the model for loop growth) versus SIMS data for the case of reduced OED.

K_{loop} was found to be 0.57. Assuming r_t=b=3.14 and r_a=2.3 as did Hu [16] yields a value for ΔH of 0.12eV. This value is much lower than 0.4 eV (4kT at 900ßC) indicating that the loop growth is only partially reaction-controlled [16]. Of course ΔH depends somewhat on the specific values chosen for r_t and r_a. Increasing r_t to 12.6 will yield 0.4 eV for the reaction barrier. On the other hand, r_t would have to be decreased to 1.7 to eliminate the reaction barrier completely. However, a toroidal radius for interstitial capture which is less than the interatomic spacing is not realistic indicating there must be a finite reaction barrier. The final simulated loop radius was 590 . Although this final loop radius is slightly lower than the average value measured in Figure 2.3 (b) (650), the total number of interstitials added to the dislocation loops is the same as the number calculated from the TEMs ($6.4x10^{14}$ cm^{-2}). The difference in final radii can be attributed to the assumption in the simulations that the dislocation loop density is constant at $4.5x10^{9}$ cm^{-2}.

The simulated results of the interstitial supersaturations at the end of the oxidation with and without extended defects are plotted in Figure 2.9. As expected, the interstitial

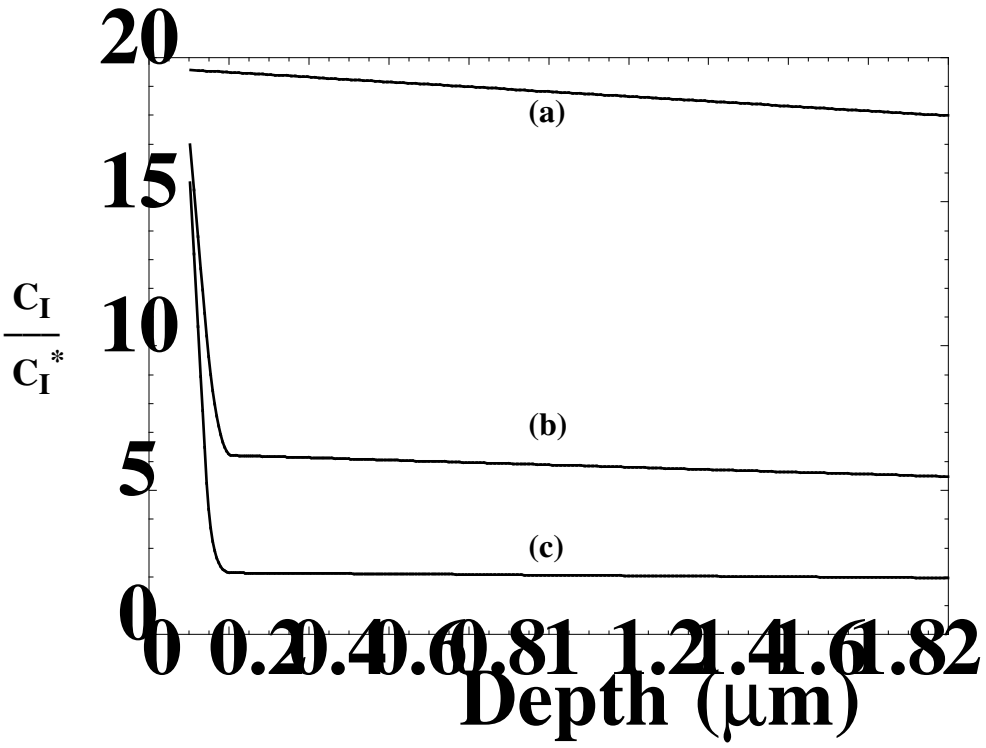

Figure 2.9 Final simulated interstitial supersaturations for the case of (a) normal OED, (b) reduced OED, and (c) diffusion-limited growth of the dislocation loops.

supersaturation is reduced when the extended defects are present. In order for loop growth to be completely diffusion-controlled, C_I/C_I^* should be approximately $C^*_{I,loop}/C_I^*$. Note that C_I/C_I^* at 0.175 μm for the simulation with extended defects (curve (b)) is approximately 6. This value is much higher than the $C^*_{I,loop}/C_I^*$ value calculated from Eq. 2.12 which is approximately 2 for a final radius of 590 (see Figure 2.6). This result indicates that the growth of the dislocation loops is not solely diffusion-limited. To investigate this further, the overall loop growth rate (Eq. 2.11) was increased by a factor of 10 above the optimized value. All other parameters remained as before and another simulation was run. The results from this simulation are also plotted in Figure 2.9. This time, C_I at the dislocation loops is approximately equal to $C^*_{I,loop}$ indicating that we have

now made the loop growth diffusion-limited. However, we have also significantly reduced the diffusion of the boron buried layer such that the simulation result no longer matches the SIMS data (see Figure 2.10). In addition, the final loop radius for the case of diffusion-

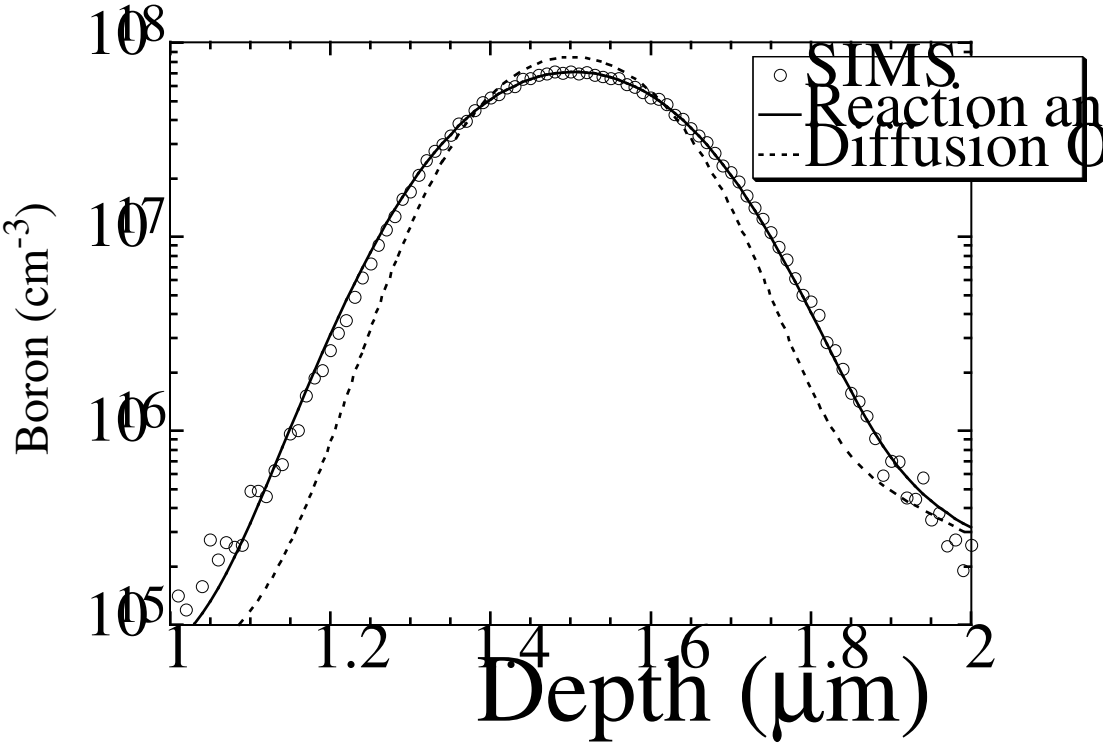

Figure 2.10 Final simulated boron profiles for the case of reaction and diffusion-controlled (solid line) and diffusion-limited only (dotted line) growth of dislocation loops compared to SIMS data.

limited growth is only 580 . The final loop radius is smaller than for the optimized case because the sink for interstitials has become so large that the injection of interstitials from the growing interface has been significantly reduced. This is seen in Figure 2.9 where the interstitial supersaturation at the interface is only 15.7 (curve (c)) as compared to 19.6 for the case of normal OED (curve (a)). Our assumption in Section 2.2.3 that the interstitial supersaturation at the growing interface is the same with or without the layer of dislocation loops is not completely valid. $s_I^{surface}$ for the optimized simulation with defects (curve (b)) is about 90% of the value for normal OED. This will only result in a slightly higher $D_I C_I^*$ product than the one calculated in Section 2.2.3.

The sensitivity of K_{loop} on the interstitial parameters listed in Table 2.2 was investigated. As long as the $D_I C_I^*$ product, the D_I/K_S^I ratio and diffusion-limited bulk

Parameter	Value
D_I	$3.031 \times 10^9 \exp(-3.66/kT)$ $cm^2 s^{-1}$
C_I^*	$1.056 \times 10^{16} \exp(-1.14/kT)$ cm^{-3} (1.5×10^{11} cm^{-3} at 900ßC)
K_S^I	$2.009 \times 10^{11} \exp(-3.455/kT)$ cm/s
D_V	$3.0 \times 10^7 \exp(-4.652/kT)$ $cm^2 s^{-1}$
C_V^*	$8.0 \times 10^{17} \exp(-0.503/kT)$ cm^{-3}
K_S^V	$5.556 \times 10^6 \exp(-3.983/kT)$ cm/s
K_B	$8 \times 10^{-8}(D_I + D_V)$ $cm^3 s^{-1}$ (diffusion-limited)
K_{rat}	2400
B/A	$1.23 \times 10^6 \exp(-1.60/kT)$ µm/hr for T <= 900ßC $1.05 \times 10^8 \exp(-2.05/kT)$ µm/hr for T >= 900ßC
B	$1.7 \times 10^4 \exp(-1.17/kT)$ μm^2/hr for T <= 950ßC $4.2 \times 10^2 \exp(-0.78/kT)$ μm^2/hr for T >= 950ßC

Table 2.2 Defect parameters used for SUPREM-IV simulations. All parameters except B, B/A, and C_I^* at 900ßC are taken from Griffin *et al.* [23]. B and B/A are taken from SUPREM-IV [7], and C_I^* at 900ßC is obtained from this work. D_I is the interstitial diffusivity, C_I^* is the equilibrium interstitial concentration, K_S^I is the inert interstitial surface recombination velocity, D_V is the vacancy diffusivity, C_V^* is the equilibrium vacancy concentration, K_S^V is the inert vacancy surface recombination velocity, K_B is the bulk recombination coefficient, K_{rat} is a constant multiplier on K_S^I used for a growing interface, B/A is the Deal-Grove linear rate oxide growth coefficient, and B is the Deal-Grove parabolic rate oxide growth coefficient.

recombination were maintained, the optimal value for K_{loop} remained essentially the same. This indicates the general form of Eq. 2.11 is correct to within a constant of multiplication.

To this point, we have explicitly used the reaction formulation of Eq. 2.11 to solve for the growth of dislocation loops. The only influence of interstitial diffusion has been the calculation of C_I at the layer of dislocation loops by SUPREM-IV. We will now implement an equation for loop growth that accounts for both the diffusion of interstitials to the loops as well as the reaction at the boundaries of the loops.

Hu also solves the steady-state diffusion problem of interstitials to a toroid with large radius, r, and small radius, r_t [16]. Assuming $r >> r_t$ (which holds for our case):

$$\frac{dr}{dt} = \frac{2\pi D_I (C_I^{\infty} - C_C)}{N_o ln(8r/r_t)} \tag{2.17}$$

where the notation remains as before with the addition of C_I^{∞}, the interstitial concentration very far from the dislocation loop (see Figure 2.5). By combining Eq. 2.11 and Eq. 2.17, we obtain the following analytic expression for C_c:

$$C_C = \frac{C_I^{\infty} + KC_{I,\,loop}^{*}}{K+1} \tag{2.18}$$

where

$$K = \frac{1}{2} K_{loop} ln\left(\frac{8r}{r_t}\right) \tag{2.19}$$

and K_{loop} remains $(r_t/r_a)^2 \exp(-\Delta H/kT)$ as before. Substituting Eq. 2.18 into either Eq. 2.11 or Eq. 2.17 yields the final expression for loop growth:

$$\frac{dr}{dt} = \left(\frac{\pi}{N_o}\right)\left(\frac{K_{loop}}{1/2K_{loop} ln(8r/r_t) + 1}\right) D_I (C_I^{\infty} - C_{I,\,loop}^{*}) \tag{2.20}$$

Equation 2.20 now accounts for both diffusion of interstitials to the stacking fault as well as the reaction that occurs at the boundary of the stacking fault. This analysis is very similar to the balance of oxidant diffusion and oxidant reaction that occurs during oxide growth on silicon. Equation 2.20 was implemented into SUPREM-IV and the interstitial

continuity equation, Eq. 2.13, was modified accordingly. The only remaining question is what value to use for C_I^{∞} in Eq. 2.20. Originally, this value was assumed to be the interstitial concentration an infinite distance away from the dislocation loop in any direction. However, during a thermal oxidation, the interstitial concentration at the growing silicon/oxide interface will have a much higher value than the concentration deep in the bulk. In this case, C_I^{∞} can certainly not be greater than C_I^{surf}, the interstitial concentration on the silicon side of the growing interface. Thus, C_I^{∞} was set equal to C_I^{surf} as a limiting case.

The same parameters given in Table 2.2 were used, but this time Eq. 2.20 was used to solve for dislocation loop growth instead of Eq. 2.11. K_{loop} was varied until the simulated boron profile matched the SIMS data for reduced OED. The final simulated radius remained 590 indicating that we have also matched the TEM data using Eq. 2.20. The optimized value for K_{loop} was 0.42. Using r_t=3.14 and r_a=2.3 as before, yields 0.15 eV for ΔH at 900ßC which is not much different from the 0.12 eV extracted using Eq. 2.11 and further supports our claim that the growth of the dislocation loops has both diffusion and reaction components.

We have now shown that either Eq. 2.11 or Eq. 2.20 can be used to simulate the reduction in OED due to the absorption of interstitials by dislocation loops. The extracted values for the reaction energy barrier are slightly different. However, we have just made the assumption that C_I^{∞} is equal to C_I^{surf} in our implementation of Eq. 2.20. In fact, C_I^{∞} must be less that C_I^{surf} which will result in a larger value for K_{loop} and therefore a smaller value for ΔH. In Eq. 2.11, we have assumed that the value at the boundary of the dislocation loop is the same as the average interstitial concentration at the layer of dislocation loops calculated by SUPREM-IV. A more precise analysis will require at least two-dimensional and possibly three-dimensional analysis of the diffusion of interstitials to an array of dislocation loops. Meanwhile, we have found that Eq. 2.11 is more stable numerically than Eq. 2.20. This is probably because C_I at the layer of dislocation loops varies over a much smaller range than does C_I^{surf}. For this reason, the simulations throughout the rest of this thesis use Eq. 2.11 (and Eq. 2.13).

One may argue that a one-dimensional model is not sufficient for modeling the growth of extended defects and thereby question our conclusion that the loop growth is partially reaction-controlled and partially diffusion-controlled. However, our conclusion does not depend on the model that we have used for dislocation growth (as evidenced by our implementation of two different equation for loop growth), but on comparison of the calculated interstitial supersaturation from the data in Table 2.1 to the calculated value from Eq. 2.12. For low dislocation loop densities (on the order of $1x10^{10}$ cm^{-2} and lower), if the growth was purely reaction-limited, then there would be no reduction in the interstitial supersaturation and the OED of the boron marker layer would have been unaffected by the presence of the loops. On the other hand, if the process was purely diffusion-limited, then the interstitial concentration near the dislocation loops would have been very close to $C^*_{I,loop}$. However, the experimental interstitial supersaturation for the case when extended defects are present is almost 6 which is still much higher than the value predicted by Eq. 2.12.

We have assumed that the interstitial profile surrounding the dislocation loops reaches a steady-state condition very quickly, but since the average distance from the surface to the layer of dislocation loops is on the order of the size of the dislocation loops, this assumption may not be valid. In the regions between the dislocation loops, the interstitial concentration may not be constant and most likely varies due to the two-dimensional diffusion that occurs around the loops. However, we justify the use of a one-dimensional model for the dislocation loop growth based on the boron SIMS data where we measure interstitial supersaturation very far away from the dislocation loops. Even though a one-dimensional model for loop growth does not capture all the kinetics involved with loop growth, we have shown that such a model can capture the key elements that are essential to arguing the consistency of our experimental results.

2.2.7 Comparison of simulation results to experimental data at other temperatures

The same methodology described in Section 2.2.6 and the same parameters as listed in Table 2.2 were used to extract the optimized values for K_{loop} at the other three

temperatures. In these simulations, an initial radius of 335 and a dislocation loop density of $2x10^9$ cm^{-2} were used based on the TEM for the initial sample shown in Figure 2.13. The optimized values for θ along with a best-fit Arrhenius expression are plotted in Figure

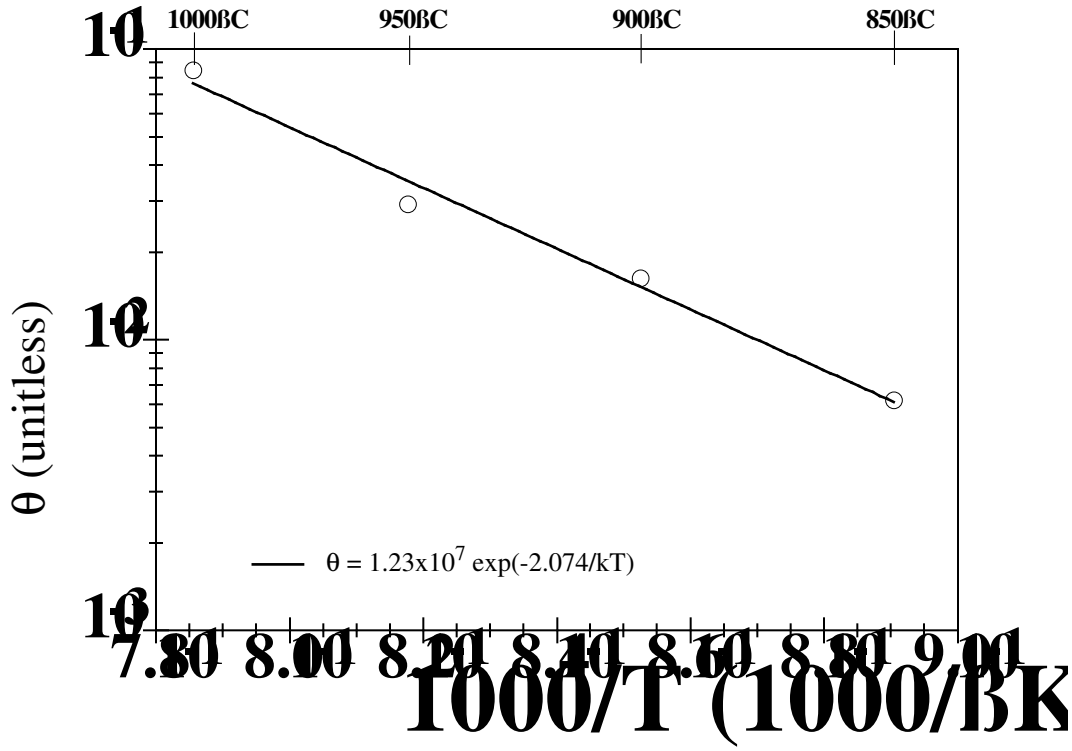

Figure 2.11 Optimized values for θ as a function of oxidation temperature. The open circles are the optimized values, and the solid line is the best-fit Arrhenius expression to all the data.

2.11. The optimized values for K_{loop} along with a best-fit Arrhenius expression are plotted in Figure 2.12. The slope of the line in Figure 2.12 represents the reaction energy barrier for dislocation loop growth. One expects this number to be negative. However, our data indicates that the reaction energy barrier is positive 1.97 eV. This contradiction is resolved when we look at the plan-view TEMs of the samples before and after oxidation in Figure 2.13. For the 950ßC and 1000ßC oxidized samples, the TEMs show that the dislocation loops have become so large that they now intersect the surface of the sample and are surface stacking faults. Our assumption that the dislocation loops grow uniformly on all sides is no longer valid. Even though no large discrepancy in oxide thickness on different

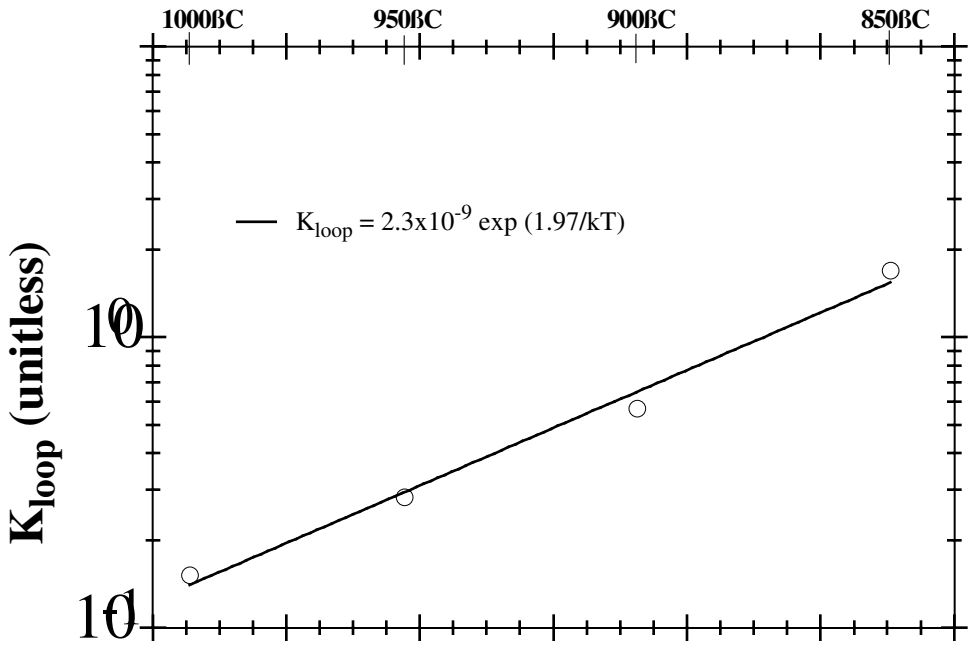

PostScript error

Figure 2.12 Optimized values for K_{loop} as a function of oxidation temperature. The open circles are the optimized values, and the solid line is the best-fit Arrhenius expression to all the data.

regions of the wafers was observed (see Table 2.1), the presence of surface stacking faults may have locally altered the oxidation kinetics. For the 850ßC oxidation, although the dislocation loops remain discrete, the TEM shows the presence of many half-loops. The exact role of these half-loops during the oxidation is very difficult to determine [24]. However, some of the injected interstitials are certainly interacting with the half-loops as well as the full dislocation loops. Our model only accounts for interaction with full dislocation loops. Thus the extracted value for K_{loop} collectively accounts for the interaction with both full and half dislocation loops.

We have found that the final defect structure observed in the TEM micrographs is a function of the initial silicon implant conditions. For the 900ßC oxidation, a single $1x10^{15}$ cm^{-2}, 100 keV implant was used to generate the surface amorphous layer while for the

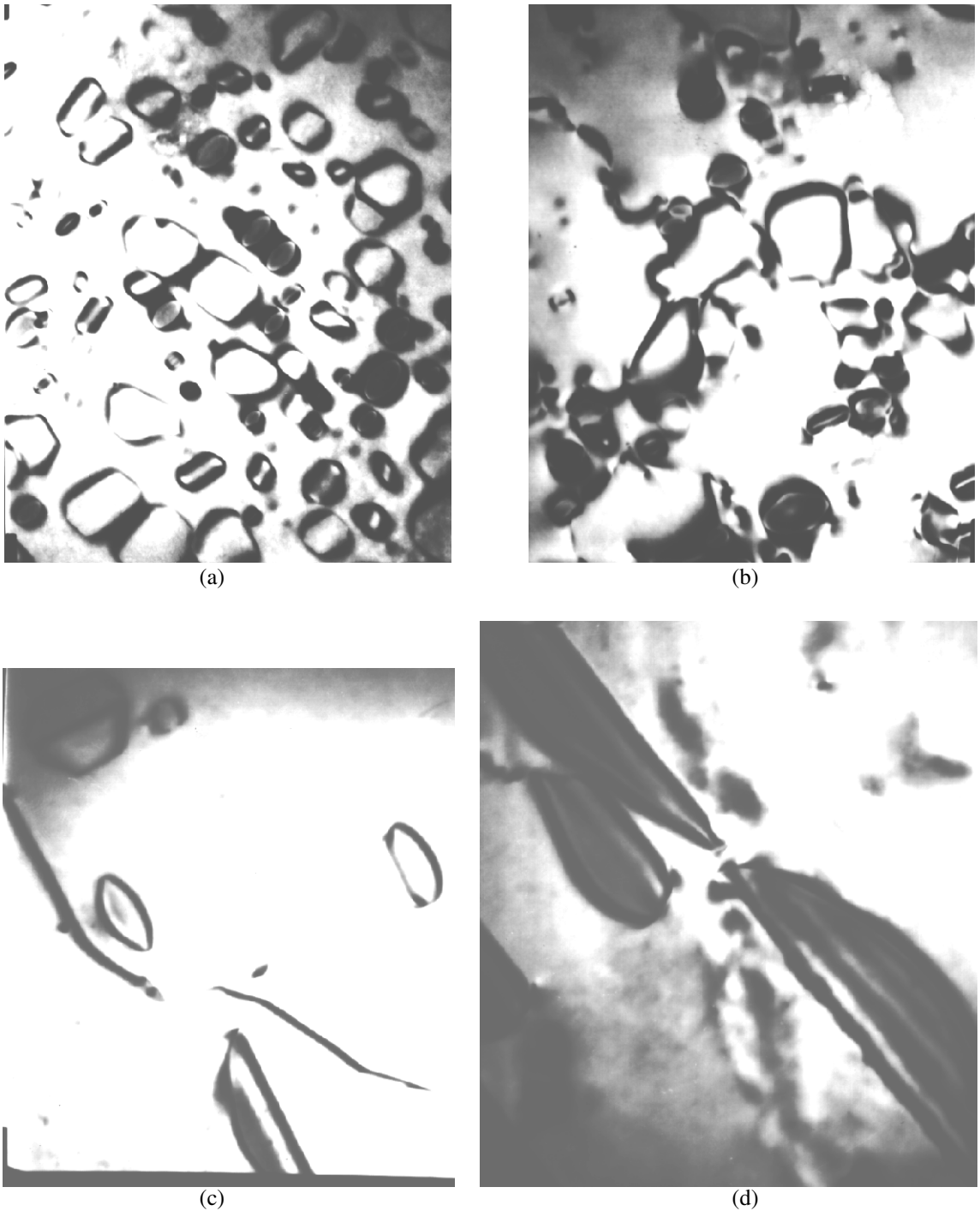

Figure 2.13 Plan-view TEM micrographs (a) before oxidation, (b) after 850ßC, 3 hour wet oxidation, (c) after 950ßC, 45 minute wet oxidation, and (d) after 1000ßC, 30 minute wet oxidation. The magnification in all pictures is 66,000X.

oxidations at other temperatures, an additional $1x10^{15}$ cm^{-2}, 50 keV implant was needed to generate surface amorphous layers.

2.2.8 Application of dislocation loop model during inert anneals

Orlowski has shown that localized sinks for interstitials can result in uphill diffusion of phosphorus during wet oxidation [25]. Using the dislocation loop model and the results from the previous sections, we demonstrate the ability of our model to predict such an effect and compare our simulated results with experimental data.

Servirdori *et al.* [26] have performed an experiment in which the silicon substrate was preamorphized by two silicon implants, one at $1.5x10^{15}$ cm^{-2}, 100 keV and the second at $5x10^{14}$ cm^{-2}, 50 keV. This generates a 2000 thick surface amorphous layer. The samples were then furnace annealed at 900ßC for 30 minutes to nucleate dislocation loops. Next, phosphorus was implanted at a dose of $2x10^{14}$ cm^{-2} and an energy of 160 keV. Then the samples were annealed at 900ßC for 3 minutes, presumably in an inert ambient. Under these conditions, the phosphorus exhibits a large amount of uphill diffusion in the region where the dislocation loops are present. Figure 2.14 compares the experimental profile from [26] to our simulation results using SUPREM-IV with the model for dislocation loops. Again, the parameter set in Table 2.2 was used in the simulations. The layer of dislocation loops was centered at 2000 , and from TEM data given in [26], the initial radius of the dislocation loops was set to 165 and the initial density was set to $3.4x10^{10}$ cm^{-2}. In addition, the as-implanted phosphorus profile was used as the initial interstitial profile at the start of the simulation. Some uphill diffusion is predicted in the simulation. However, the amount of uphill diffusion is much larger in the experimental data. The fact that the phosphorus doping level is above the intrinsic carrier concentration (n_i is $4x10^{18}$ cm^{-2} at 900ßC) in this experiment complicates matters. The effect of high concentration diffusion is at least as important as the effect of the dislocation loops on the final phosphorus distribution. A more desirable experiment would be one in which the doping level is well below n_i at the anneal temperature. Park and Law have recently done such an experiment [31]. In their experiment, a constant $3x10^{17}$ cm^{-2} boron background was used as the starting condition. Silicon was implanted into the substrate at $2x10^{15}$ cm^{-2}, 150 keV

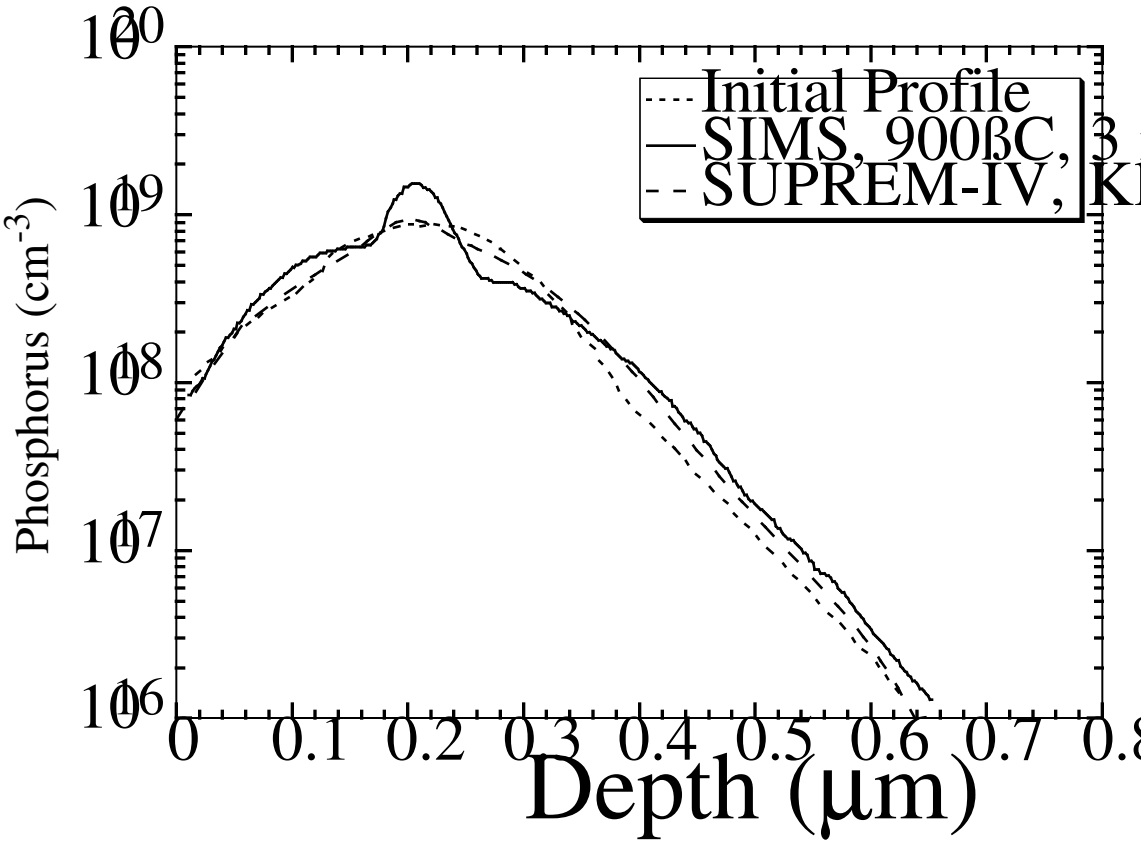

Figure 2.14 Comparison of experimental data for uphill phosphorus diffusion from [26] to a SUPREM-IV simulation using the model for dislocation loop growth.

and at $6x10^{14}$ cm^{-2}, 80 keV to generate a surface amorphous layer approximately 1700 thick. The samples were then annealed in an inert ambient, and uphill diffusion was observed for anneals between 800ßC and 900ßC.

Figure 2.15 compares the experimental data to simulations using our model for the growth of dislocation loops. Again, the parameters in Table 2.2 were used in the simulations, and because no information was given on the initial starting condition of the dislocation loops, the initial size and density of dislocation loops was assumed to be the same as what was used for simulating the reduced OED at 900ßC (namely, r_{init}=235 and

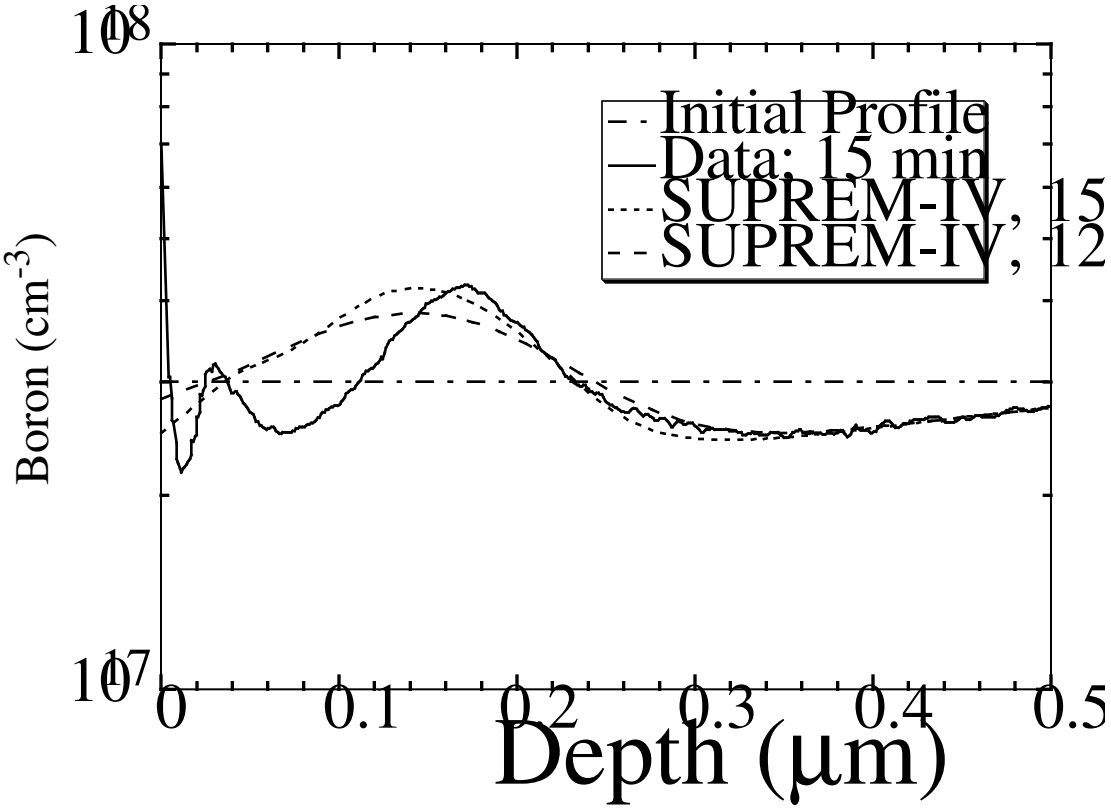

Figure 2.15 Comparison of uphill boron diffusion from [31] to simulations using SUPREM-IV and the model for the growth of dislocation loops.

ρ=4.5x10^9 cm^{-2}). The same value for K_{loop} extracted for the reduced OED data at 900ßC was used in the simulation in Figure 2.15. Finally, for the initial interstitial profile, the implanted silicon profile beyond the amorphous layer was obtained via a Boltzmann Transport Equation (BTE) solver [27],[28]. Since the amorphous layer regrows in less than a second at 900ßC [29], we have assumed that the interstitial concentration has returned to equilibrium in the previously amorphous silicon layer, and that the only remaining excess interstitials are those beyond the amorphous layer. The initial interstitial profile used in the simulation is shown in Figure 2.16. We have used this same approach to calculate the initial interstitial concentration in previous work [30]. The agreement between the SIMS data and the simulation is very good, especially for the boron depletion beyond the amorphous layer. The SIMS data also shows that the boron does not move significantly from the 15 minute annealed profile out to 120 minutes [31]. This is

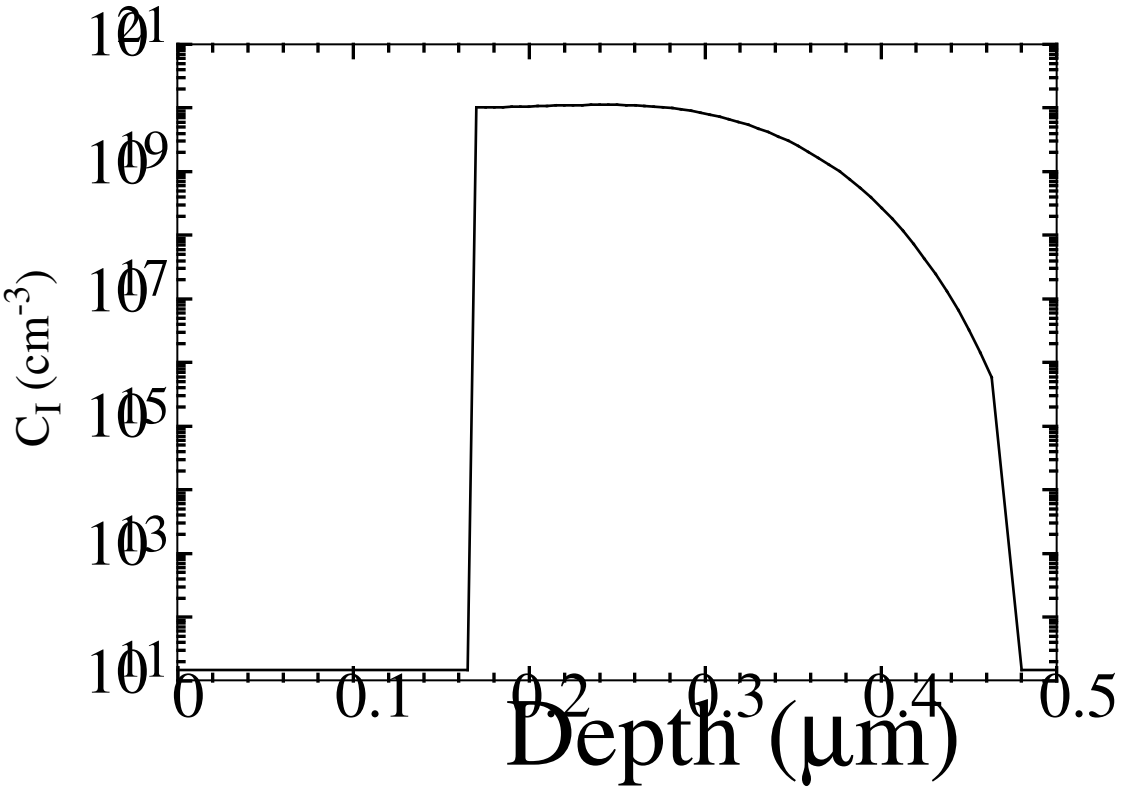

Figure 2.16 Initial interstitial concentration used in the simulation that generated the final boron profile shown in Figure 2.15.

successfully modeled in Figure 2.15. The small boron hump in the experimental data very close to the surface was attributed to another layer of dislocation loops [31]. We have not tried to simulate this secondary layer of loops in Figure 2.15. The influence of this secondary layer, the lack of information regarding the location, initial radius, and density of the dislocation loops, and the uncertainty in the initial interstitial concentration all contribute to the disagreement between the simulation result and the experimental data in the surface region.

2.2.9 Comparison of dislocation loop model to other models

In this section, we compare our model for dislocation loop growth to other models that have recently been proposed.

2.2.9.1 Orlowski s model

Orlowski [25] has modelled the effect of dislocation loops by adding a term to the interstitial continuity equation of the form $-\alpha g(x)(C_I-C_I^*)$, where α characterizes the strength of the interstitial sink and g(x) characterizes the sink distribution. g(x) is given by $\exp\{-[(x-x_d)/w_d]^2\}$ where x_d is the center location of the dislocation loops and w_d is the width of the layer containing the dislocation loops. This model is very similar to the model which we first implemented in [14] in which we added the term $-K_{int}(C_I-C_I^*)$ to the interstitial continuity equation which was effective only within a specified region. In both Orlowski s model and our original model, there was no attempt to determine an analytic closed-form expression for the sink coefficient (α in Orlowski s model and K_{int} in our model).

2.2.9.2 Park s model

Park *et al.* have also developed a model for the growth of dislocation loops based on the stress fields generated by the dislocation loops [32]. First we will enumerate the key features of their model, then contrast their model to ours.

1. They assume regular two-dimensional arrays of dislocation loops. From the arrays of dislocation loops, the effective pressure due to the loops is calculated in one-dimension, vertically into the substrate. The calculated one-dimensional pressure profile is then used to calculate new values for C_I^*, C_V^*, D_{AI}, and D_{AV}, the equilibrium interstitial and vacancy concentrations, and the dopant/interstitial and dopant/vacancy pair diffusivities, respectively.
2. They account for the statistical distribution of the dislocation loops through the following equation for N, the number of interstitials trapped in all the dislocation loops:

$$N = \frac{\pi N_o}{24} m L_p^{-2} [\,(R_p + R_{max})\,(R_p + R_{min}) + R_{max}^2 + R_{min}^2] \qquad (2.21)$$

where the parameters are defined as follows:

$N_{o:}$ {111} planar density of silicon
m: sampling period of dislocation loop radii
L_p: characterizes the density of the majority size loops
D_p: $0.5L_p^{-2}$
R_p: radius of the majority size loops
R_{max}: radius of the largest size loops
R_{min}: radius of the smallest size loops.

The change in N as a function of time is modeled via:

$$\frac{dN}{dt} = \{\frac{\partial N}{\partial R_p} + \frac{\partial N}{\partial L_p}\frac{dL_p}{dR_p} + \frac{\partial N}{\partial R_{min}} + \frac{dR_{min}}{dR_p} + \frac{\partial N}{\partial R_{max}}\frac{dR_{max}}{dR_p} + \frac{\partial N}{\partial m}\frac{dm}{dR_p}\} (\frac{\partial R_p}{\partial t}) \quad (2.22)$$

3. The interstitial and vacancy continuity equations are modified to use:

$$\frac{\partial C_X}{\partial t} = \nabla \left[D_X C_X^*(P) \nabla \left(\frac{C_X}{C_X^*(P)} \right) \right] - R_{bulk} - K_{XL}(C_X - C_{X,loop}^*) \quad (2.23)$$

where X represents either point defect I or V, $C_X^*(P)$ represents the new equilibrium defect concentration due to the pressure P, K_{XL} represents the sink coefficient for point defects, and $C^*_{X,loop}$ represents the equilibrium defect concentrations at the loop layer boundary. Furthermore, the parameters K_{IL} and K_{VL} are coupled to the change in N via:

$$\frac{dN}{dt} = \alpha K_{IL}(C_I - C_{I,loop}^*) - \alpha K_{VL}(C_V - C_{V,loop}^*) \quad (2.24)$$

In contrast to Park s model, we do not consider pressure effects. However, localized pressure changes due to the dislocations change the equilibrium point defect concentrations and the dopant/point defect pair diffusivities by a factor of 25% or less [31]. The effects of the internal energy of the stacking fault as well as the strain energy of the stacking fault (see Eq. 2.12) on equilibrium point defect concentrations are much larger than this. Also, in the last section, we have shown that we can model the effect of uphill boron diffusion without consideration of the pressure effect.

In our model, we have assumed that all the loops have the same average radius, r, and that the density of the loops remains constant with time. Park uses a triangular distribution to statistically describe the size and density of dislocation loops. Although the second approach is more correct physically, our approach is simpler because the only required inputs are the location of the dislocation loops, their average radius, and their average density. In Park s model, one must also extract from the TEM data partial derivatives necessary to evaluate Eq. 2.22.

In Park s model, the change in N is related to the interstitial continuity equation through the additional parameter α. In our model, the change in N is explicitly accounted for through an analytic expression which accounts for the reaction of interstitials at the dislocation loop boundary. No additional fitting parameters are necessary to relate the change in N to the interstitial continuity equation. While we have ignored any contribution to loop kinetics due to vacancies, Park accounts for the interaction of vacancies with dislocation loops by adding an analogous term for vacancies, $K_{VL}(C_V - C^*_{V,loop})$, to the vacancy continuity equation. However, there is currently no experimental data with which to extract K_{VL}, and in fact, Park uses a value for K_{VL} which is seven orders of magnitude less than K_{IL} [33].

To summarize, both models presented here for dislocation loop growth are essentially one-dimensional models. The basic effect of either model is the addition of a term to the interstitial continuity equation of the form $K_{int}(C_I - C^*_{I,loop})$. The two models simply use different approaches to account for the interstitials absorbed by the loops.

2.3 Effects of Extended Defects After Additional Implant Damage

2.3.1 Introduction

Analogous to the case of reduced OED, in this section we investigate the ability of extended defects to reduce enhanced diffusion of a boron marker layer after low-dose silicon implants. Servidori *et al.* [26] have observed reduced diffusion of phosphorus

layers after implantation into preamorphized silicon and postulated the reduction was due to the interaction of point defects with extended defects. In this section, we confirm their hypothesis using our own experimental data.

2.3.2 Experimental Procedure

The starting material was 4-inch, 5-10 Ω-cm CZ, <100>, phosphorus-doped silicon. Silicon epitaxy at 800ßC was used to grow a $1x10^{18}$ cm^{-3} boron layer followed by a lightly doped arsenic layer. A low-temperature oxide was deposited at 400ßC and used to mask half of the wafers. The wafers were then implanted with Si^{28} at an energy of 100 keV and a dose of either $1x10^{13}$ cm^{-2} or $2x10^{15}$ cm^{-2}. The masking oxides on the wafers were stripped in an HF acid solution, and the wafers were then rapid thermal annealed (RTA) at 1050ßC for 1 minute. Si^{28} was implanted a second time across the entire wafer at a dose of $2x10^{14}$ cm^{-2} and an energy of 70 keV, and another low-temperature oxide was deposited as a cap layer. Half of each wafer was saved for initial profile measurements, and the other half was furnace annealed at either 750ßC for 2 hours or 900ßC for 30 minutes in an argon ambient. Samples initially implanted with different doses of Si^{28} were annealed at the same time ensuring identical thermal treatment. The experimental matrix is given in Table 2.3. Samples were bevelled at a shallow angle [34] and stained with copper sulfate in a dilute HF solution to delineate p-n junctions [35]. In addition, oxides were etched off, and initial and final boron profiles were measured using SIMS with an oxygen primary beam in a CAMECA IMS-4f system. A summary of the process flow is given in Figure 2.17.

Sample ID	First silicon implant dose	Final Anneal	<D>/D* (unitless)
H2-Mask	$2x10^{15}$ cm^{-2}	750ßC, 120	1110
H2-Open	$2x10^{15}$ cm^{-2}	750ßC, 120	660

Table 2.3 Experimental matrix along with extracted time-averaged enhanced diffusivities. Open regions were exposed to the first silicon implant while Mask regions were masked from the first implant by a thick oxide. <D> is the time-averaged boron diffusivity, and D* is the default value for inert boron diffusivity in SUPREM-IV. [7]

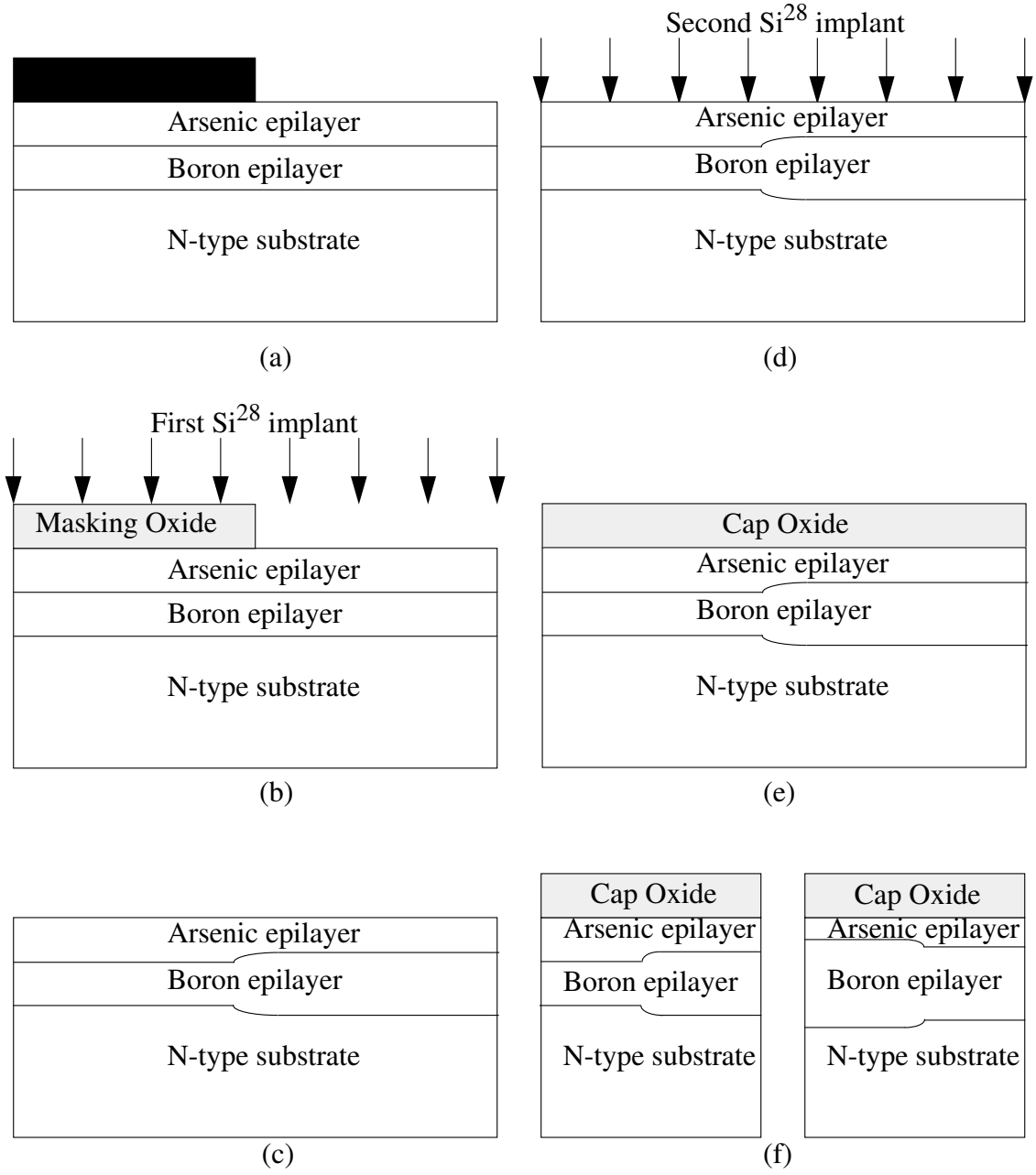

Figure 2.17 Process flow for reduced IED study. (a) After epitaxial growth, oxide deposition, and lithography. (b) $1x10^{13}$ cm^{-2} or $2x10^{15}$ cm^{-2}, 100 keV Si^{28} implant. (c) After oxide etch and 1050ßC, 1 minute rapid thermal anneal. (d) Second Si^{28} implant, $2x10^{14}$ cm^{-2}, 70 keV. (e) After final oxide deposition. (f) Wafers cleaved in half. Half saved for initial profiles (left side) and half furnace annealed at either 750ßC for 2 hours or 900ßC for 30 minutes in an argon ambient (right side).

Sample ID	First silicon implant dose	Final Anneal	<D>/D* (unitless)
H3-Mask	$1x10^{13}$ cm^{-2}	750ßC, 120	1100
H3-Open	$1x10^{13}$ cm^{-2}	750ßC, 120	1120
H5-Mask	$2x10^{15}$ cm^{-2}	900ßC, 30	15.5
H5-Open	$2x10^{15}$ cm^{-2}	900ßC, 30	10.5

Table 2.3 Experimental matrix along with extracted time-averaged enhanced diffusivities. Open regions were exposed to the first silicon implant while Mask regions were masked from the first implant by a thick oxide. <D> is the time-averaged boron diffusivity, and D* is the default value for inert boron diffusivity in SUPREM-IV. [7]

2.3.3 Experimental Results

Figure 2.18 shows the bevel-and-stain result for sample H2 which was initially implanted with a $2x10^{15}$ cm^{-2} dose of silicon. The copper stains n-type material and, as seen in Figure 2.18 (a), because of implantation damage from the first silicon implant, the p-n junction is slightly deeper underneath the implanted region as compared to the masked region (note that the top junction was not detectable using this technique). This same result was observed for samples H3 and H5 as well. However, after the second silicon implant and subsequent furnace anneal on H2 (Figure 2.18 (b)), the p-n junction is now deeper underneath the region masked from the first implant. Extended defects created by the high-dose implant and subsequent RTA absorb some of the interstitials generated by the second implant, reducing the normal enhanced diffusion of the boron layer which is observed in the masked region. In comparison, for sample H3, initially implanted with a low-dose ($1x10^{13}$ cm^{-2}) of silicon, the final junction depth is the same across the entire wafer implying that the initial low-dose implant did not significantly affect the enhanced diffusion from the second silicon implant. These results are similar to the reduced OED effects observed in Section 2.2.2. The bevel-and-stain results are verified by the SIMS data shown in Figure 2.19, Figure 2.20, and Figure 2.21 for samples H2, H3, and H5, respectively. SUPREM-IV was used to extract time-averaged enhanced diffusivities of the boron for the three different samples with the results shown in Table 2.3. The default value

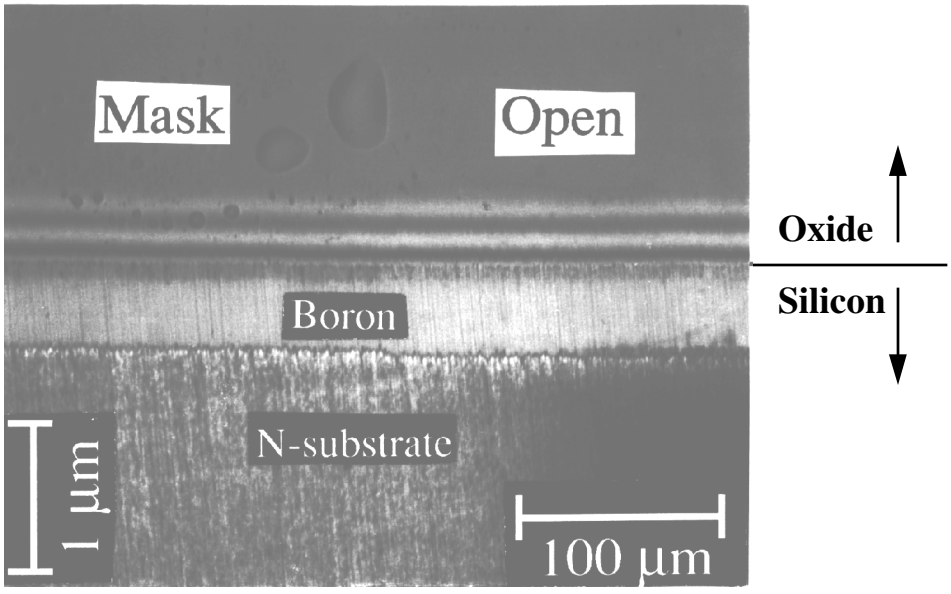

(a)

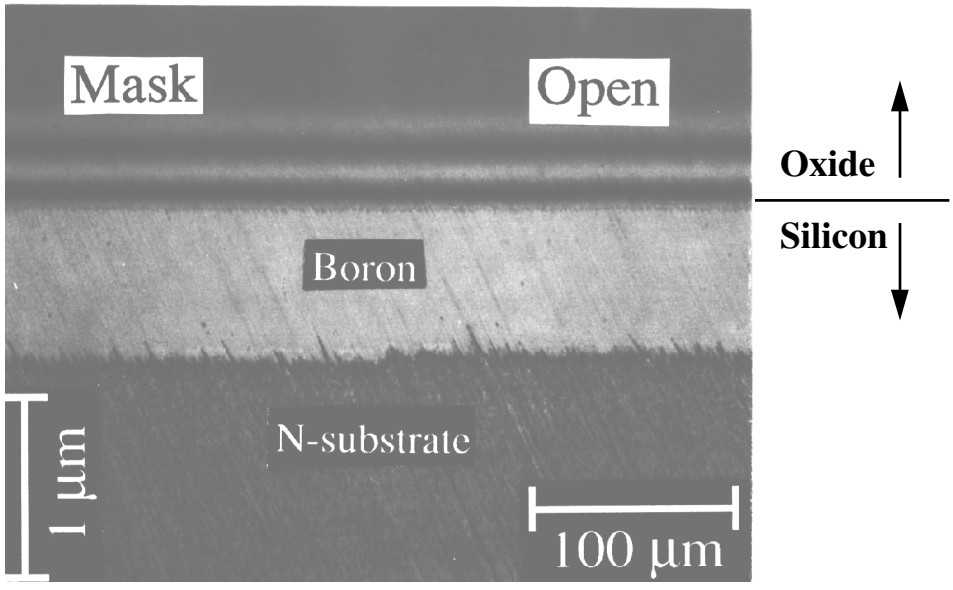

(b)

Figure 2.18 Bevel-and-stain result on sample H2 (a) before final anneal, (b) after 750ßC, 2 hour inert anneal.

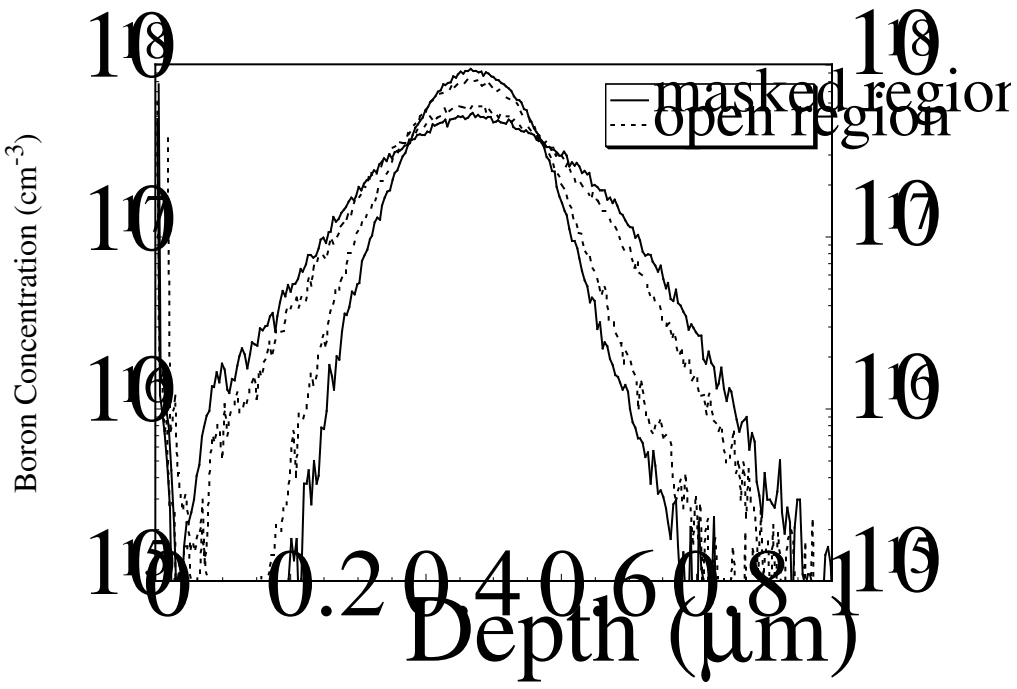

Figure 2.19 SIMS boron data of sample H2 which was first implanted with $2x10^{15}$ cm^{-2}, 100 keV Si^{28}, RTA annealed, implanted again with a low-dose of Si^{28}, then furnace annealed at 750ßC for 2 hours. The solid lines are data taken from a masked region and the dotted lines are from an open region.

for inert boron diffusivity in SUPREM-IV [7] was assumed to be correct in these simulations.

The reduced diffusion observed under heavily-implanted regions in Samples H2 and H5 is due to the absorption of implant-generated interstitials by extended defects. A channeling RBS measurement confirms the existence of a buried amorphous layer after the $2x10^{15}$ cm^{-2}, 100 keV silicon implant from 750 to 1670 below the surface. According to Jones *et al*. [8], Type-IV defects, also called clamshell or zipper defects, form whenever a buried amorphous layer is produced. In addition, Type-II defects will form whenever an amorphous layer (buried or surface) is generated. Type-IV and Type-II defects are both extrinsic dislocation loops having different crystal orientations.

In summary, we have shown that extended defects are also effective at reducing IED. Similar to the case for the reduction of OED, the reductions in enhancement are larger for lower temperature anneals.

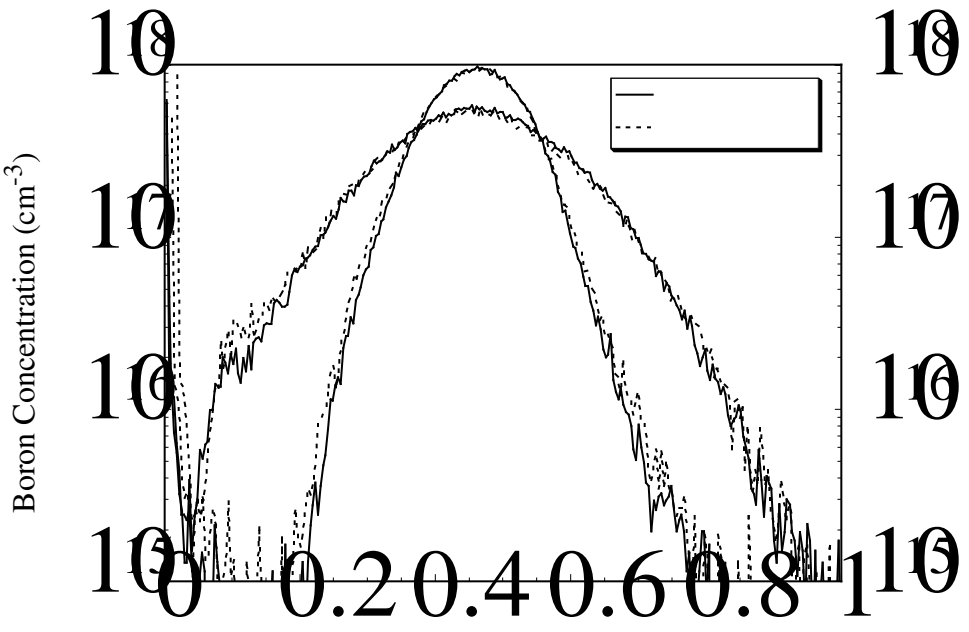

PostScript error

Figure 2.20 SIMS boron data of sample H3 which was initially implanted with $1x10^{13}$ cm^{-2}, 100 keV Si^{28}, RTA annealed, implanted again with a low-dose of Si^{28}, then furnace annealed at 750ßC for 2 hours. The solid lines are data taken from a masked region and the dotted lines are from an open region.

2.4 Summary

In this chapter, we have experimentally shown that extended defects generated by amorphizing implants affect point defect concentrations during subsequent processing steps. In particular, we have shown that extended defects are effective at reducing OED as well as IED of a boron marker layer grown via silicon epitaxy. We have also described a one-dimensional model for dislocation loop growth which was implemented into SUPREM-IV, and we used this new model in SUPREM-IV to successfully simulate reduced OED due to the absorption of injected interstitials by the dislocation loops. We also showed that the growth of implant-induced stacking faults is both diffusion and reaction-controlled. We then showed that the model for dislocation loops can successfully predict uphill diffusion. Finally, we compared our model for dislocation loop growth to other recently proposed models.

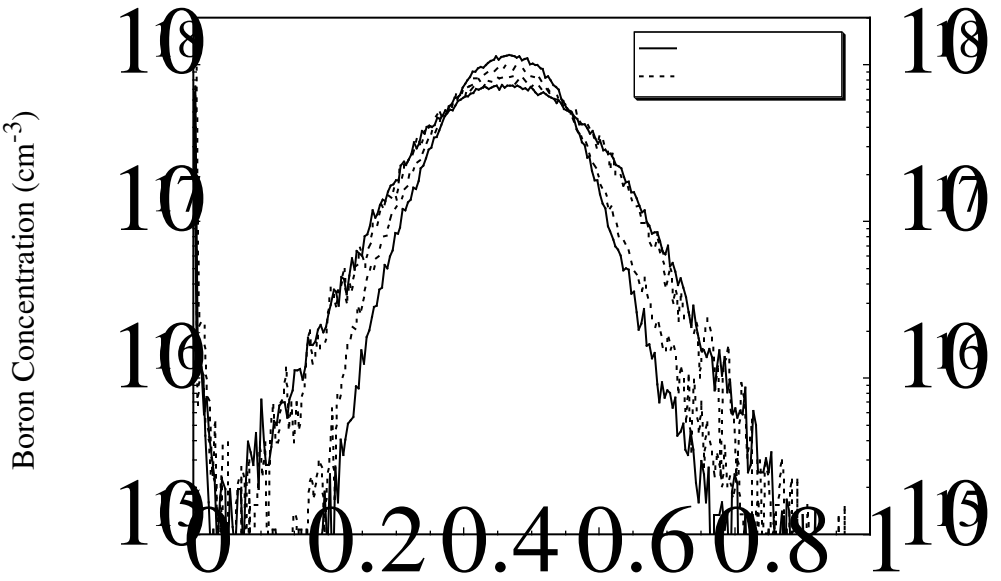

Figure 2.21 SIMS boron data of sample H5 which was initially implanted with $2x10^{15}$ cm^{-2}, 100 keV Si^{28}, RTA annealed, implanted again with a low-dose of Si^{28}, then furnace annealed at 900ßC for 30 minutes. The solid lines are data taken from a masked region and the dotted lines are from an open region.

PostScript error

FrameMaker has detected one or more PostScript errors in this document.
()
Please check your output.